2

Short Introduction to Flight Trajectories for Aerothermodynamicists

Aerothermodynamic design, aerothermodynamic phenomena, and the choice of flight trajectories of either re-entry vehicles, space-transportation systems or hypersonic aircraft depend mutually on each other. We give here a short introduction to issues of flight trajectories in order to provide basic knowledge about these dependencies.

The very fast flight of hypersonic vehicles, partly with vast changes of the flight altitude, makes a precise flight guidance necessary. This is especially a problem with CAV-type space transportation systems because of their very small pay-load fractions. The basic problem is to find a flight trajectory which permits the vehicle to fulfill its mission with minimum demands on the vehicle system. However, different from classical aircraft design, the physical properties and the functions of a hypersonic vehicle and its components must be extremely closely tailored to the flight trajectory and vice versa.

To design and to optimize a vehicle's flight trajectory in a sense is to solve a guidance problem. While the fulfillment of the basic mission is the primary objective of the trajectory definition, other, secondary objectives may exist. In the multi-objective design and optimization of a trajectory, these must be identified as **guidance objectives**. It is further necessary to define and to describe the **trajectory control variables**, which permit the vehicle to fly the trajectory. Finally, a system reduction is necessary to identify a few characteristic physical loads and vehicle properties/functions, whose limitations and/or fulfillments are introduced as **systems and operational constraints** in the trajectory design and optimization process. The eventual outcome are **guidance laws**, which in general have a rather small number of free parameters to fulfill the mission objectives under the given conditions.

Prerequisites for trajectory design and optimization are flyability and controllability of the considered vehicle on the sought trajectory. Under flyability we understand longitudinal trimmability, and static and dynamic stability, which, with a few exceptions, is the rule for both the longitudinal and the lateral motion of the vehicle. Controllability is the ability to steer the vehicle around all relevant vehicle and air-path related axes with the help of control devices. For RV-W's these are aerodynamic control surfaces and usually, in addition, reaction control systems (RCS) in the form of small rocket thrusters located appropriately around the vehicle, for RV-NW's they are in general

solely reaction control systems.[1] We stress the fact that only a "trimmed" trajectory is a viable trajectory. For airbreathing (CAV) flight vehicles the influence of the thrust vector of the propulsion system in the lift-drag plane on the longitudinal force and the moment balance must be taken into account.

Trajectory design and optimization must allow for uncertainties in the describing data of the vehicle, its sub-systems, and the flight environment, for a RV-W see, for instance [1]. The uncertainties concern the aerodynamic model—the aerodynamic data set—of the vehicle including uncertainties in the performance data of the control devices, and also uncertainties in the performance data of the propulsion system in the case of CAV's. Uncertainties of other kinds are present as a rule regarding the vehicle mass, the location of the center-of-gravity of the flight vehicle and its moments of inertia. This holds especially for RV-NW's with ablation cooling. With CAV's all these are anyway not constant because of the fuel consumption during flight, and, in the case of TSTO-systems, also because of the separation of the upper stage.

Other uncertainties come in from the sensor systems (air data, acceleration data) etc., and are also given in the form of deviations from the, for the trajectory design chosen, standard atmosphere during the actual mission, especially regarding the density ρ_∞, and the possible presence of wind. The latter concerns in particular CAV's, because these fly predominantly in the troposphere and the stratosphere, Appendix B.

In the following sections we look at the trajectory design and optimization elements which have close connections to aerothermodynamics (guidance objectives, trajectory control variables, systems and operational constraints). We consider the forces acting on a vehicle, discuss the equilibrium glide trajectory of RV-W's and RV-NW's (the compact and frame-consistent derivation of the general equations for planetary flight is given at the end of the chapter), give qualitative results, and show in case studies some examples of trajectories. We refrain from discussing guidance laws, and refer the reader the reader instead to, e.g., [2]. We begin with RV-W's and RV-NW's, where considerable flight experience is available,[2] and proceed with CAV's, where, however, flight experience is not available.

[1] The major role, however, of the RCS of a flight vehicle leaving the atmosphere (above $H \approx 80$ to 100 km) and/or performing orbital flight, is to carry out orbital manoeuvering.

[2] The reader is especially referred to [1] about the Space Shuttle Orbiter's reentry guidance.

2.1 Flight Trajectories of Winged and Non-Winged Re-Entry Vehicles

2.1.1 General Aspects

RV-W's and RV-NW's have in common that their re-entry flight as decelerating flight is actually a braking mission. Their large initial total air-path energy

$$E_{t,i} = m\left(gH_i + \frac{1}{2}v_i^2\right), \tag{2.1}$$

is dissipated exclusively by means of the aerodynamic drag. In eq. (2.1) m is the vehicle mass, g the gravitational acceleration as function of the altitude, Section C.1, H_i the initial altitude, and v_i the initial speed.

The dissipation of the large initial total energy requires specific systems constraints of which the dynamic pressure, the thermal surface loads and the aerodynamic load factor belong to the most important ones. The result is an usually very narrow re-entry flight corridor. We show in Fig. 2.1 as an example the flight corridor of the Space Shuttle Orbiter for the operational angle of attack profile [1].

The minimum weight of the Space Shuttle Orbiter's thermal protection system (TPS) is achieved by flying on a large part of the trajectory the maximum angle of attack, consistent with the cross-range requirements, in order to minimize the thermal loads. During the initial five flights, which

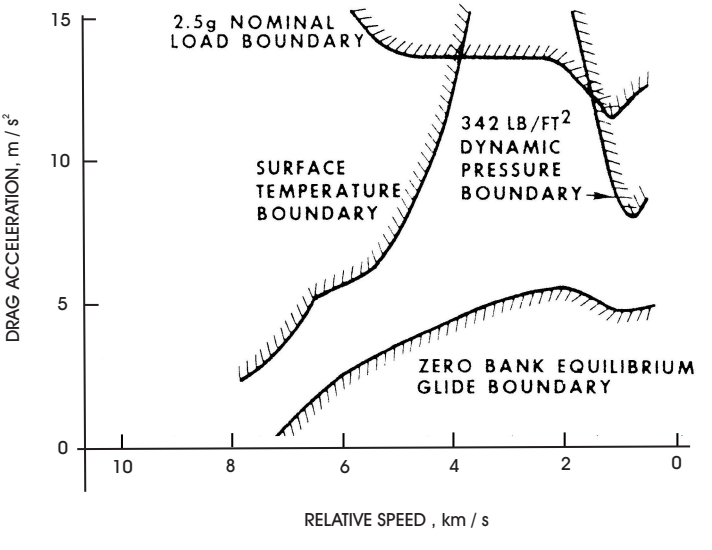

Fig. 2.1. Flight corridor of the Space Shuttle Orbiter (operational flights) [1].

served as test flights, this angle was $\alpha = \alpha_{max} = 40°$, during the following operational flights $\alpha = \alpha_{max} = 38°$ [1].

A RV-W flies, with basically fixed configuration, in a large Mach number and altitude range. During the high speed re-entry it flies at large, and at low Mach numbers at small angles of attack. With increasing angle of attack the effective longitudinal "nose" radius in the stagnation point region of the vehicle increases (rise of effective bluntness).[3] With increasing nose radius, at constant flight speed and altitude, the boundary layer thickness increases and the thermal loads, both the heat flux in the gas at the wall, q_{gw}, and the surface temperature T_w (which without slip-flow effects is equal to the temperature in the gas at the wall T_{gw}, Section 9.1) of the radiation cooled TPS surface, decrease [5].

Increased effective bluntness also increases the portions of the bow shock with large inclination against the free-stream, and hence the wave drag and with that the deceleration[4] of the vehicle along the flight path. The blunt vehicle shape at large angle of attack thus serves both low thermal loads and high drag (and deceleration) [5].

The flight trajectories of RV-W's and RV-NW's can be distinguished in the altitude-velocity map, Fig. 2.2. The lift parameter $\alpha_W = W/(A_{ref}C_L)$ and the ballistic parameter $\beta_W = W/(A_{ref}C_D)$ are derived in Sub-Section 2.1.4. They can be related to each other by the lift-to-drag ratio L/D. The "lifting" re-entry trajectory of RV-W's is much "higher" than that of RV-NW's. Our intuition tells us that the higher the trajectory, the smaller the thermal loads, but the lower the effectiveness of aerodynamic stabilization, trim, and control surfaces. The ballistic or semi-ballistic re-entry of RV-NW's thus is marked by much larger thermal loads than the lifting re-entry of RV-W's.

Cross-range capabilities of RV-W's and especially RV-NW's are limited because of their small lift-to-drag ratios. Usually RV-W's have in the high speed domain a $L/D = \mathrm{O}(1)$ due to the blunt vehicle shape and the large angles of attack. The Space Shuttle Orbiter has a trimmed $L/D \approx 1$ at $\alpha \approx 40°$, Fig. 2.3[5] [7]. For the upper stage HORUS of the TSTO reference concept SÄNGER of the former German Hypersonics Technology Programme, [8], $L/D \approx 1.9$ was envisaged at that angle of attack. For RV-NW's we find $L/D = 0.1$ to 0.3 [9], which is achieved by an offset of the center-of-gravity from the centerline, and hence is the trimmed L/D. For purely ballistic re-entry

[3] For the Space Shuttle Orbiter's equivalent axisymmetric body, [3], the "nose" radius rises almost linearly from $R_N = 0.493$ m at $\alpha = 21.8°$ to $R_N = 1.368$ m at $\alpha = 42.75°$ [4].

[4] In trajectory design and optimization the term "drag acceleration" is used instead of the term "deceleration", Sub-Section 2.1.4.

[5] The agreement between the flown L/D data of the trimmed vehicle and the predicted data is very good. The flight data show Mach number independence, Section 3.6.

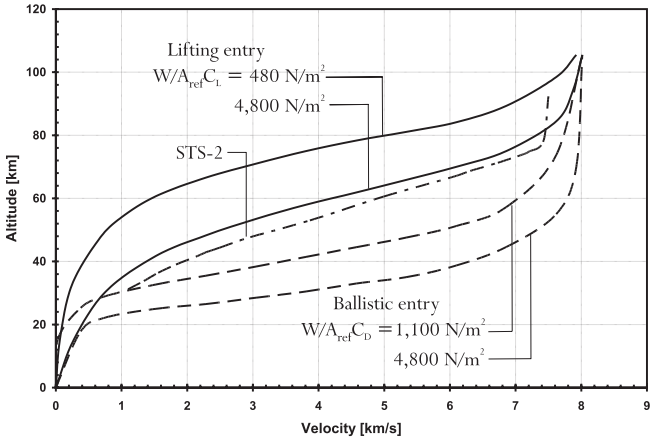

Fig. 2.2. Trajectories of RV-W's and RV-NW's with typical values of lift parameters and ballistic parameters in the altitude-velocity map (STS-2: second flight of the Space Shuttle Orbiter, data from [6]).

capsules $L/D = 0$. All these vehicles can be considered as compressibility or pressure effects dominated flight vehicles, Section 1.1.

Lift-to-drag ratios of O(1) of RV-W's are due to the blunt, although elongated shape of the vehicles—usually with large portions of the lower side being approximately flat, Sub-Section 3.2.2—in combination with large angles of attack.

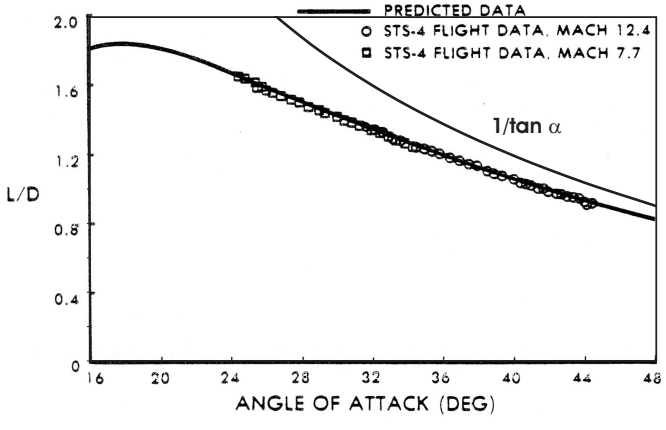

Fig. 2.3. Trimmed lift-to-drag ratio L/D of the Space Shuttle Orbiter in the hypersonic domain as function of the angle of attack α [7]. The large angle of attack interval of the flight data was achieved by transient pushover-pull-up maneuvers around the actual flight angle of attack.

During a re-entry flight, which is performed at large angles of attack, L/D can be increased by both reducing the angle of attack α (reduction of the "effective" bluntness of the configuration) and the actual nose bluntness (nose radius R_N). If we approximate the lower side of a RV-W by an equivalent flat plate, the RV-W-type RHPM-flyer, Section 10.1, and apply Newton's theory, we find for the lift-to-drag ratio $L/D = 1/tan\,\alpha$, which in the case of the Space Shuttle Orbiter is a fair approximation for $\alpha \gtrapprox 25°$, Fig. 2.3. Thus reducing the angle of attack, also for realistic vehicle shapes, is an effective means to increase the lift-to-drag ratio, as is amply demonstrated by Fig. 2.3.

We note, however, that in reality a reduction of L/D of a given flight vehicle is undertaken on appreciable parts of the trajectory via a reduction of L. With the bank angle μ_a of the vehicle an effective lift $L_{eff} \leqq L$ and/or a side force is achieved, which serve as trajectory-control means, Sub-Section 2.1.2.

2.1.2 Guidance Objectives, Trajectory Control Variables, and Systems and Operational Constraints

We discuss now some issues of the above mentioned guidance objectives, trajectory control variables, and systems and operational constraints.

Guidance Objectives: For RV-W's and RV-NW's the most important guidance objectives are:

– **Minimization** of the **time-integrated heat flux** in the gas at the wall $\overline{q}_{gw}$ at selected reference locations

$$\overline{q}_{gw} = \int_{t_0}^{t_{flight}} q_{gw} dt, \tag{2.2}$$

which is used as a measure of the thickness and hence the weight of the heat protecting or insulating structure. The reference locations are at least the nose cap, approximated by a sphere, where q_{gw} would be the forward stagnation point heat flux, and usually parts of the TPS, where the heat fluxes q_{gw} can be approximated by those of a flat plate or a swept cylinder etc. (see, e.g., [10]). Simple relations for the estimation of q_{gw} are provided in Chapter 10.

The use of the time integral of q_{gw} in trajectory design and optimization has historical roots. In reality, it is the time integral of q_w, the heat flux which actually enters the TPS or the hot primary structure, which is of importance. In presence of radiation cooled surfaces, Section 9.1, which are the rule for hypersonic vehicles in the velocity and altitude range considered in this book, this heat flux is $q_w = q_{gw}$ - q_{rad}, where q_{rad} is the radiation cooling heat flux q_{rad}.

– **Cross range** achievement. The cross range is the lateral distance of the prescribed landing site from the exit orbital plane. Both the down range—in direction of the trace of the exit orbit plane—and the cross range are

to be achieved by a proper timing of the de-orbiting impulse. For both ranges possible cross and down winds must be compensated. In general a multi-objective problem exists, because possible contingency returns of the flight vehicle must be considered, too. In all cases the vehicle with its mass m must arrive at the terminal area (TA) with an adequate total air-path energy state—$E_{t,TA} = m_{TA}(g\,H_{TA} + 0.5v_{TA}^2) \geqq E_{TA,min}$—and a reasonable vehicle attitude.

Trajectory control variables are the attitude variables which permit to fly a RV-W or a RV-NW on its re-entry trajectory. For RV-W's most experience about vehicle control is available from the flights of the Space Shuttle Orbiter (see, e.g., [1]). In principle only three vehicle trajectory control variables are at one's disposal:

- The **angle of attack** α is the trajectory control variable of RV-W's which first of all governs the thermal loads on the vehicle's structure. In general it holds, the larger α, the smaller are these loads. The angle of attack further governs the drag and hence the deceleration of the vehicle (Sub-Section 2.1.4). The larger α, the larger is the total drag D of the vehicle. The Space Shuttle Orbiter flies at large Earth-relative speed (4 km/s $\lessapprox$ $v_\infty \lessapprox$ 8 km/s, equivalent to 12 $\lessapprox$ $M_\infty \lessapprox$ 28) at $\alpha = \mathrm{O}(40°)$ [1]. A mission usually is flown with a predefined function $\alpha(v_\infty)$. If bank angle changes or reversals are performed on the trajectory, small deviations around $\alpha(v_\infty)$ are the rule.

  For (axisymmetric) RV-NW's overall thermal loads on the front shield are smallest, if the angle of attack, Chapter 5, is zero (ballistic entry). Then also the drag is largest. However, in this case $L/D = 0$, and the cross range—without attitude-change capability—cannot be modulated.
- To modulate the effective aerodynamic lift L_{eff} $(= L\cos\mu_a$, Sub-Section 2.1.4), and the effective lift-to-drag ratio L_{eff}/D of RV-W's and RV-NW's, a **bank angle** μ_a is employed.[6] On a large (initial) part of the trajectory, changes of the angle of attack are usually not available to modulate the lift, because α must be large in order to minimize the thermal loads (see above). A large α is further needed for sufficient drag and hence vehicle deceleration.

  The bank angle in addition is the primary means to control the cross range of a vehicle. Because it directs part of the lift sidewards $(L\sin\mu_a)$, it induces a lateral motion. We see from this, that RV-NW's need to have a $L/D > 0$, i. e., to fly at angle of attack, if a cross range modulation is wanted. If the bank angle is used to reduce the flight time, and the lateral

[6] The bank angle option holds also for RV-NW's for rolling around the velocity vector even though these vehicles have axisymmetric shapes, see Fig. 2.22. This option implies a non-zero angle of attack which anyway is necessary in order to achieve a $L/D > 0$, Chapter 5.

motion is unwanted, bank angle reversals are used to compensate for it. The Space Shuttle Orbiter employs bank angles up to $\mu_a = \pm 80°$ [1].

The bank angle μ_a is defined as roll angle around the velocity vector $\underline{v}_\infty$, Fig. 2.22, of the RV-W or the RV-NW (also called air-path vector [11], or wind vector), and not as roll angle around the longitudinal axis of the vehicle. Roll must be made around the vehicle's velocity vector, otherwise the lift is not effectively modulated or directed sidewards. Further, regarding RV-W's, the lower side of the vehicle with its TPS must always remain the vehicle's windward side. On the trajectory for such vehicles, the initial bank angle is zero, i.e., $\mu_a = 0$, in other words, the wings are in horizontal position. Otherwise, the vehicle will fly inverted if $\mu_a = 180°$.

– The **sideslip (yaw) angle** β of a flight vehicle is a potential trajectory control variable. But because it would induce unwanted increments of thermal loads, at least in the high Mach number segment of the trajectory, sideslip should be zero on a large part of the trajectory, i. e. the vehicle should fly at high speed with $\beta = 0$.

Systems and operational constraints: For both RV-W's and RV-NW's several systems and operational constraints exist. They may influence only parts of the trajectory or the whole trajectory.[7] We list the most important flight path systems and operational constraints of both vehicle types. For details regarding especially RV-W's we refer the reader to, e.g., [1].

– The **dynamic pressure** q_∞ is one of the most important systems and operational constraints with:

$$q_\infty = \frac{1}{2}\rho_\infty v_\infty^2 \leqq q_{\infty,max}. \tag{2.3}$$

The dynamic pressure is a measure of the mechanical (pressure and shear stress) loads on the vehicle structure, mainly the surface pressure. Important is that also all aerodynamic forces and moments are proportional to it. This holds also for performance and efficiency of aerodynamic stabilization and control devices and the sizes of the hinge moments of aerodynamic trim and control surfaces, which govern the actuator performance.

For RV-W-type's the maximum allowed dynamic pressure typically chosen is about $q_{\infty,max} \approx 14$ kPa, which amounts to the maximum value of the Space Shuttle Orbiter [12]. Initially on a re-entry trajectory q_∞ is much lower due to the low density, see the X-38 example in Sub-Section 2.1.7. This leads to the problem of reduced and insufficient effectiveness of aerodynamic stabilization, trim and control surfaces. To overcome this problem, reaction control devices, as in the case of the Space Shuttle Orbiter (see, e.g., [13]) are employed. There, the vertical RCS jets operate in roll for $q_\infty \lessapprox 0.48$ kPa ($H \gtrapprox 81$ km, $M_\infty \gtrapprox 27$), and in pitch for $q_\infty \lessapprox 1.9$ kPa ($H \gtrapprox$

[7] In any case not only the nominal flight trajectory must be considered, but conceivable alternative trajectories, and especially abort trajectories.

69 km, $M_\infty \gtrapprox 22$). The yaw RCS jets are active as long as $M_\infty > 1$. The body flap and the elevons are active at $q_\infty \gtrapprox 0.1$ kPa ($H \lessapprox 90$ km, $M_\infty \lessapprox 27$), the rudder only at Mach numbers $M_\infty \lessapprox 5$, where at angles of attack $\alpha \lessapprox 20°$ to 25° the vertical stabilizer begins to leave the "shadow" of the fuselage.[8]

For RV-NW's a large range of maximum dynamic pressures can be found from low values like 6.2 kPa for OREX up to 25 kPa for the lunar return of APOLLO and even larger ones.

– **Thermal loads**[9] must be sufficiently low so that the thermal protection system can cope with them, and functions and integrity of all other structural elements are not deteriorated.

The maximum permissible thermal loads must be seen relative to the considered locations on the flight vehicle. The structure and materials concept of, e.g., the TPS, or of a control surface etc., always is tailored closely to the expected and actual thermal (and mechanical) loads in order to save weight and cost. The thermal loads are very different at the different locations of the vehicle. This holds even for the TPS, whose thickness decreases from the forward part of thew vehicle (maximum) towards the aft part (minimum). Behind this fact is the behavior, Chapter 9, of the heat flux in the gas at the wall, q_{gw}, and the wall temperature T_w in the presence of radiation cooling, which in general is quite close to the radiation-adiabatic temperature T_{ra}, Section 9.1.

Trajectory design and optimization in general is made using a heat flux as constraint, either the total heat flux Q_∞, eq. (2.4), or, as the rule, the heat flux in the gas at the wall q_{gw} (see the guidance objectives above) at one or more reference locations as a result of the mentioned system reduction. The reference locations are usually and primarily the nose cap, which is approximated by a sphere (forward stagnation point of the vehicle), and in addition other configuration parts[10], which can be approximated by swept cylinders (leading edges) or flat plates (flat portions of the lower side), etc. (see, e.g., [10]). At the sphere, for instance, it is demanded that $q_{gw} \lessapprox q_{gw,max}$, with, depending on the overall structure and material layout of the vehicle, $q_{gw,max} = 400$–$1{,}200$ kW/m^2.

The requirement that q_{gw} at the reference locations remains within given constraints $q_{gw,max}$, holds for the whole configuration on the nominal flight trajectory and on all conceivable alternative trajectories, including abort

[8] The vertical stabilizer has the drawback that it is not effective at the high angles of attack which are flown on a large part of the trajectory. However, it must be seen in the frame of the overall vehicle and mission layout, which is a result of numerous design trades.

[9] We define thermal loads, Chapter 9, in the sense that they encompass both surface temperatures T_w and the heat flux into the surface q_w [5].

[10] In [5] it is shown that, due to strong interaction phenomena, thermal loads at wing leading edges, represented in that case by the radiation-adiabatic temperature, can be as large as at the forward stagnation point of the vehicle.

trajectories. What actually is demanded, and that is the problem of a proper system reduction, is that everywhere at the vehicle and at any time the thermal loads in the form of the wall temperature T_w (in view of material strength and endurance, also with regard to erosion, where the wall shear stress τ_w plays a role, too), and the heat flux q_w into the wall, as well as the time integrated wall heat flux $\overline{q}_w$, eq. (2.2), are within the limits of the given vehicle layout.[11] To check whether this requirement is met, appropriate post-optimization analyses of the trajectory must be made.

The total heat flux Q_∞ is the heat transported per unit area and unit time towards a flight vehicle:

$$Q_\infty = \rho_\infty v_\infty \left(h_\infty + \frac{v_\infty^2}{2} \right), \tag{2.4}$$

with ρ_∞ and v_∞ being the free-stream density and speed (their product is the mass flux per unit area towards the flight vehicle), and h_∞ the enthalpy of the free-stream, i. e., of the undisturbed atmosphere.

At hypersonic speed the kinetic energy is dominant, and hence the transported heat is approximately proportional to the flight velocity squared, and we note:

$$Q_\infty \sim \rho_\infty v_\infty \frac{v_\infty^2}{2} \sim q_\infty v_\infty. \tag{2.5}$$

The heat flux in the gas at the wall, q_{gw}, of a sphere usually is approximated with the help of the relation of Fay and Riddell, Section 10.3. For the computation of large amounts of trajectory points, simpler relations for q_{gw} of the type

$$q_{gw} = C_{gw} \rho_\infty^n v_\infty^m, \tag{2.6}$$

for spheres, swept cylinders, flat plates, the latter two for both laminar and turbulent (flight below approximately 60 to 40 km altitude [5]) flow, can be found, Section 10.3. For relations for flat surfaces see, e.g., Section 10.4. For spheres $n = 0.5$ to 1, and $m \gtrapprox 3$. C_{gw} must be chosen accordingly. For a sphere, for instance, it includes the inverse of the square root of the radius, $(1/\sqrt{R})$, Section 10.3.

We remind the reader that for the actual structure and materials layout the heat flux into the wall q_w, respectively the time-integrated value $\overline{q}_w$ is the relevant one. The wall temperature T_w is of equal importance as q_w, [5], because it determines the choice of the material. It must be below the

[11] For the development of the Aeroheating Design Data Base of the Space Shuttle Orbiter the following major reference locations were distinguished [10]: the fuselage lower side including the nose area, the wing lower surface, the wing leading edges, control surfaces, the wing lee side, the fuselage sides and its upper surface.

maximum permissible one: $T_w \leqq T_{w,max}$. For radiation cooled surfaces the radiation-adiabatic temperature T_{ra} in general is a good approximation of the real T_w. Transverse and tangential heating through the structure must be considered in non-convex or transverse situations, see Section 9.1 and Sub-Section 6.3.3 respectively. These heating issues are further discussed in Sub-Section 8.4.3. With the approximate relations for T_{ra} given in Chapter 10, it can easily and with acceptable cost be checked, whether on the trajectory $T_w \leqq T_{w,max}$ is fulfilled at the reference locations.

– The normal **load factor** is defined as the ratio of the normal aerodynamic force $N = q_\infty C_N A_{ref}$ to the vehicle weight $W = m\,g$:

$$n_z = \frac{q_\infty C_N A_{ref}}{m\,g},$$

where, following [11], g should be taken as function of the distance of the actual flight path to the center of Earth: $g = g(R_E + H)$, where R_E is the mean Earth radius and H the flight altitude, Appendix C. It concerns the loads on the flight vehicle structure as well as on the passengers and the payload. The constraint is $n_z \lessapprox n_{z,max}$, and the maximum value is usually defined for RV-W's as $n_{z,max} = 2$–2.5, while for RV-NW's it can reach $n_{z,max} = 8$–10.

– **Equilibrium glide**, Sub-Sections 2.1.4 and 2.1.5, is associated with the minimum drag acceleration if the bank angle is zero, and is used as operational constraint, too.
– **Trimmability** can be considered as indirect operational constraint which partly is covered by the dynamic-pressure constraint. It must be assured on the whole trajectory. It can have severe implications for the trajectory. If, for instance, a large trim-surface (e.g. body flap) deflection is needed on a large part of the trajectory, the ensuing trim drag will influence the down and the cross range of the vehicle. Also influenced are the hinge moments (demands on actuator performance), and the mechanical and thermal loads of the trim surface, which then pose additional systems and operational constraints.
– **Stability and controllability**, like trimmability are also indirect operational constraints. Forces exerted by aerodynamic stabilization and control surfaces can pose systems and operational constraints, either by being too large or too small. If, for instance, at high altitudes aerodynamic stabilization and control surfaces are not effective, a RCS must be foreseen, see the "dynamic pressure" constraint.

2.1.3 Forces Acting on a Re-Entry Vehicle

We consider a RV-W on its flight path. We summarize the axes, forces and moments in Table 2.1, following [11]. The general axis convention is: the x-axis in both the body-axis and the air-path axis system points forward, the

Table 2.1. Axes, and aerodynamic forces (in brackets the "aerodynamic" notation) and moments (all are right-hand orthogonal triples) in the body-axis system and the air-path system [11].

Axis system	Axis	Force	Moment
Body axis			
	longitudinal axis x	axial force X (A)	rolling moment L^A
	lateral axis y	side force Y	pitching moment M^A
	normal axis z	normal force Z (N)	yawing moment N^A
Air-path axis			
	air-path axis x_a	drag X_a (D)	rolling moment L_a
	air-path lateral axis y_a	lateral force Y_a (C)	pitching moment M_a
	air-path normal axis z_a	lift Z_a (L)	yawing moment N_a

z-axis downward, and the y-axis to the right, when looking in flight direction (see Fig. 7.1 and [14]–[17]). Both axis systems are right-handed systems. The definition of the forces is given in Fig. 7.2.

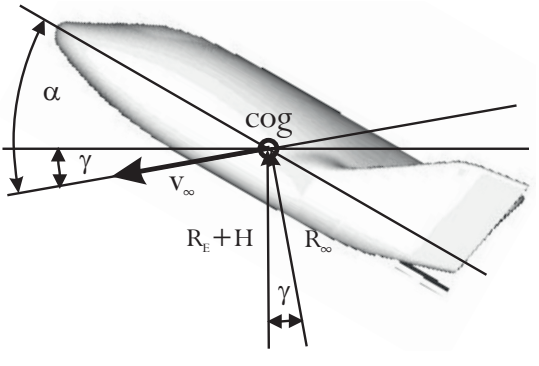

Fig. 2.4. Schematic of a re-entry vehicle on its flight path (cog: center-of-gravity). $R_E + H$ is the distance to the center of Earth, R_∞ is the local radius of the curved flight path. γ is the flight-path angle.

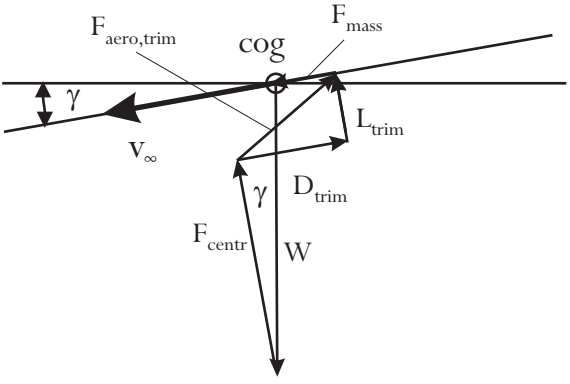

Fig. 2.5. Schematic point-mass force polygon at re-entry flight (the aerodynamic forces are those of trimmed flight, $F_{aero,trim}$ is the resultant aerodynamic force of trimmed flight).

The aerodynamicists, however, usually have the x-axis pointing backward, the z-axis upward, and the y-axis to the right, when looking in flight direction, see, e.g., Fig. 7.3. We use this convention throughout the book.[12]

For the pitching moment in the body-axis system usually and also in this book the symbol M is used instead of M^A. In Chapter 5 the more convenient notation $[L, M, N]$ is used for the components of the moment vector.

The vehicle has a weight W, acting on it is the aerodynamic lift L, the aerodynamic drag D, and the centrifugal force F_{centr} ("g-reduction" due to the high speed flight on a curved trajectory). Moreover, at a CAV also the inlet drag force and the thrust force of the propulsion system act on the vehicle, Section 2.2.3. In non-steady flight an inertial or mass force F_{mass} complements these forces. The flight path is inclined by the flight path angle γ against the local horizontal plane, which is defined positive in upward direction and negative in downward direction, Fig. 2.4. The angle γ varies along the flight path. The flight vehicle is approximated as a point mass, i. e., it is trimmed, but moments are not examined[13].

The forces acting on the vehicle are shown in Fig. 2.5. The flight path angle γ initially is small (γ = O(- 1°)) (danger of phugoid motion of the vehicle[14]), and varies in general only little down to approximately 40 km altitude.

---

[12] The reader is generally warned, that it is mandatory and absolutely necessary, when using data and literature from other disciplines, or when dealing with representatives of other disciplines, that a full understanding and agreement is reached about axis conventions, symbols, signs, and nomenclature!

[13] For trim and stability considerations see Sub-Section 3.4.2

[14] Long-period lightly damped oscillatory modes are called phugoid motion (see, e.g., [18].

2.1.4 The Equilibrium Glide Trajectory

The equilibrium glide trajectory is defined as having a small flight path angle γ which does not change with time, see below. Hence it is not a viable trajectory, because in reality γ is small only on the initial trajectory and $d\gamma/dt \neq 0$. However, the equilibrium glide trajectory is very useful, because it permits to obtain a closed solution for the flight speed as function of the flight time. From this several important, though in general qualitative results can be found, which we discuss in Sub-Section 2.1.5.

In Section 2.3 we present a compact and frame-consistent derivation of the general equation for unpowered planetary flight, which results in three scalar equations, eq. (2.55), see also [19]. By assuming that the vehicle moves in a great-circle plane (this means a non-rotating Earth: $\omega = 0$) and the flight path azimuth angle χ is constant, we have for "planar" flight[15], Fig. 2.5:

$$\frac{dv_\infty}{dt} = -\frac{D}{m} - \frac{W}{m}\sin\gamma = -\frac{D}{m} - g\sin\gamma = -\frac{F_{mass}}{m}, \tag{2.7}$$

$$v_\infty \frac{d\gamma}{dt} = \frac{1}{m}L - \frac{W}{m}\cos\gamma + \frac{v_\infty^2}{R_\infty} = \frac{1}{m}L - g\cos\gamma + \frac{v_\infty^2}{R_\infty}, \tag{2.8}$$

where $m = W/g$ is the vehicle mass[16], g the gravitational acceleration, which is a function of the flight altitude, Appendix C, and $R_\infty = (R_E + H)/\cos\gamma \approx R_E + H$, the local radius of the flight path. R_E is the mean Earth radius, H the flight altitude, and, compared to eq. (2.55), we have the identities $v_\infty \equiv V$ and $R_E + H \equiv r$.

To describe and evaluate flight trajectories with eqs. (2.7) and (2.8), the kinematic relations for the altitude H and the longitudinal angle θ are needed, too, see eq. (2.52):

$$\frac{dr}{dt} \equiv \frac{d(R_E + H)}{dt} = \frac{dH}{dt} = V\sin\gamma, \tag{2.9}$$

and

$$r\frac{d\theta}{dt} \equiv (R_E + H)\frac{d\theta}{dt} = V\cos\gamma. \tag{2.10}$$

The third term on the right-hand side of eq. (2.8) times the vehicle mass m is the centrifugal force F_{centr} due to the curved trajectory of the flight vehicle:

$$F_{centr} = m\frac{v_\infty^2}{R_\infty}. \tag{2.11}$$

For flight control and guidance purposes the lift vector $\underline{L}$ can be rotated out of the planar surface by the bank angle μ_a, Section 2.3 and Sub-Section 2.1.2.

[15] The subscript 'trim' of L and D in Fig. 2.5 for convenience is omitted in this and in the following equations.

[16] The reader should note, that W is not the weight of the vehicle at sea level, because $g = g(H)$, Appendix C.

In this case we replace L by $L\cos\mu_a$, which is then the component of the lift acting against the Earth gravitation. We call this the effective lift L_{eff}:

$$L_{eff} = L\,cos\mu_a. \tag{2.12}$$

The bank angle also serves to create the side force $L\,sin\mu_a$ needed for cross range control, see Sub-Section 2.1.2 and third equation of eq. (2.55).

Introducing the aerodynamic force coefficients C_L and C_D, and the reference area A_{ref}, yields from the above relations after rearrangement the with g normalized acceleration along the flight path:

$$n_t = \frac{1}{g}\frac{dv_\infty}{dt} = -sin\gamma - \frac{\rho_\infty v_\infty^2}{2}\left(\frac{W}{A_{ref}C_D}\right)^{-1}, \tag{2.13}$$

and normal to it:

$$n_n = \frac{v_\infty}{g}\frac{d\gamma}{dt} = \frac{\rho_\infty v_\infty^2}{2}\left(\frac{W}{A_{ref}C_L}\right)^{-1} - cos\gamma + \frac{1}{g}\frac{v_\infty^2}{R_\infty}. \tag{2.14}$$

The terms in brackets are the ballistic parameter, also called ballistic factor:

$$\beta_W = \frac{W}{A_{ref}C_D}, \tag{2.15}$$

and the lift or glide parameter:

$$\alpha_W = \frac{W}{A_{ref}C_L}. \tag{2.16}$$

The two parameters are given in terms of the vehicle weight $W = mg$. Their dimensions are $[\mathrm{M/L\,t^2}]$. In the literature they are often expressed in English units: $[\mathrm{lb_f/ft^2}]$ [20]. In metric units they read $[\mathrm{N/m^2}] = [\mathrm{Pa}]$.

If the parameters are defined in terms of the vehicle mass $m = W/g$, the ballistic parameter is:

$$\beta_m = \frac{m}{A_{ref}C_D}, \tag{2.17}$$

and the lift or glide parameter:

$$\alpha_m = \frac{m}{A_{ref}C_L}. \tag{2.18}$$

Their dimensions are in this case $[\mathrm{M/L^2}]$. In the literature they are expressed usually in metric units: $[\mathrm{kg/m^2}]$.

Ballistic and glide parameter are related to each other via the lift-to-drag ratio:

$$\frac{W}{A_{ref}C_D} = \frac{W}{A_{ref}C_L}\frac{C_L}{C_D}. \tag{2.19}$$

For RV-W's they are around[17] $W/A_{ref}C_D$ = 3,600–4,000 Pa, and if, for instance, $C_L/C_D \approx 0.8$ in the hypersonic domain at high angle of attack (α = O(40°)), $W/A_{ref}C_L \approx$ 4,500–5,000 Pa, Fig. 2.2. RV-NW-type vehicles have ballistic parameters between $W/A_{ref}C_D$ = 300 and 4,300 Pa, Tab. 5.1, see also Fig. 2.2.

The velocity change (deceleration) follows from eq. (2.7) as:

$$\frac{dv_\infty}{dt} = -\frac{D + W sin\gamma}{m} = -\frac{D}{m} - g sin\gamma, \tag{2.20}$$

where D/m is called "drag acceleration".

The flight path angle γ is small on a considerable portion of a lifting entry trajectory and, in addition, changes only slowly. Equilibrium glide flight hence is defined as flight in the limit $d\gamma/dt = 0$, with γ being small, such that sinγ ≈ 0, and cos$\gamma \approx 1$, *and* by zero bank angle μ_a.

We assume now $R_\infty = R_E$ and $g = g_0$. With the introduction of the circular or orbital speed, i.e.—disregarding aerodynamic forces—the speed of a body near the surface of Earth, which keeps it in orbit:

$$v_c = \sqrt{g_0 R_E}, \tag{2.21}$$

and after rearrangement of the above eqs. (2.13) and (2.14), we find:

$$\frac{dv_\infty}{dt} = -g_0 \frac{D}{L}\left(1 - \frac{v_\infty^2}{v_c^2}\right), \tag{2.22}$$

where

$$1 - \frac{v_\infty^2}{v_c^2} = \frac{L}{W} = \frac{\rho_\infty v_\infty^2}{2}\frac{A_{ref}C_L}{W}. \tag{2.23}$$

Combining eqs. (2.22) and (2.20), the drag acceleration of equilibrium glide flight reads

$$\frac{D}{m}|_{equilibrium\ glide} = \frac{g_0(1 - v_\infty^2/v_c^2)}{L/D}\ (= -\frac{dv_\infty}{dt}), \tag{2.24}$$

indicating that an equilibrium glide trajectory has minimum drag level, and hence can be associated with the maximum down range capability.

As we have seen in Sub-Section 2.1.2, several systems and operational constraints are to be regarded. The drag acceleration of equilibrium glide therefore is considered as the lower limit of drag acceleration on the trajectory:

$$\frac{D}{m}|_{trajectory} \geqq \frac{D}{m}|_{equilibrium\ glide}. \tag{2.25}$$

[17] This is the approximate value for the Space Shuttle Orbiter. For L/D of the Space Shuttle Orbiter as function of α see Fig. 2.3.

If L/D is fixed, for instance, due to a prescribed angle of attack, a larger drag acceleration can only be attained with a non-zero bank angle: $\mu_a \neq 0$, which means $L_{eff} < L$. This is the commonly used praxis in trajectory design and optimization.[18]

Eq. (2.22) can be integrated by separation of variables (see, e.g., [18]) to yield the flight speed v_∞ on the equilibrium glide trajectory as function of time t :

$$\frac{v_\infty}{v_c} = tanh\left(-\frac{g_0}{v_c}\frac{t}{L/D}\right) + C. \tag{2.26}$$

In [18], $v_\infty/v_c = 0$ at $t = 0$, which yields $C = 0$, so that the time must be counted negative.

These considerations hold for RV-W's and RV-NW's, for the latter, if $L/D > 0$. For purely ballistic RV-NW's with $L/D = 0$, similarly elements of the re-entry trajectory can be described (see, e.g., [18]).

2.1.5 Equilibrium Glide Trajectory: Qualitative Results

Re-entry flight is not made on an equilibrium glide trajectory. Initially a trajectory with a small and time-dependent flight path angle $\gamma = O(-1°)$ may be flown [9], later a pseudo-equilibrium glide may be attained [18].

Nevertheless, the above considerations allow to gain a number of qualitative insights regarding the trajectory and the aerothermodynamic phenomena and design problems. The following results must be understood in the sense that small increments of a variable lead to bounded increments of the dependent variable, while the other involved variables remain in principle unchanged. Therefore, for instance, the dependence of the lift L and the drag D on the dynamic pressure q_∞ is not explicitly noted. Large increments of a variable may lead to fundamental changes of the trajectory, which would change the whole picture.

– Combining eq. (2.23), for instance, with eq. (2.6), gives a relation for the heat flux in the gas at the wall at an appropriate reference location of the vehicle:

$$q_{gw} = C_{gw}\left(\frac{2W}{A_{ref}C_L}\right)^n \left(1 - \frac{v_\infty^2}{v_c^2}\right)^n \left(\frac{v_\infty}{v_c}\right)^{m-2n} v_c^{m-2n}. \tag{2.27}$$

We see that q_{gw} depends inversely on some power of the lift coefficient C_L. This coefficient increases in the considered angle of attack domain at all Mach numbers with α. Hence increasing α decreases q_{gw}, and a RV-W

[18] The concept of pseudo-equilibrium glide takes into account a time-varying lift due to a finite bank angle.

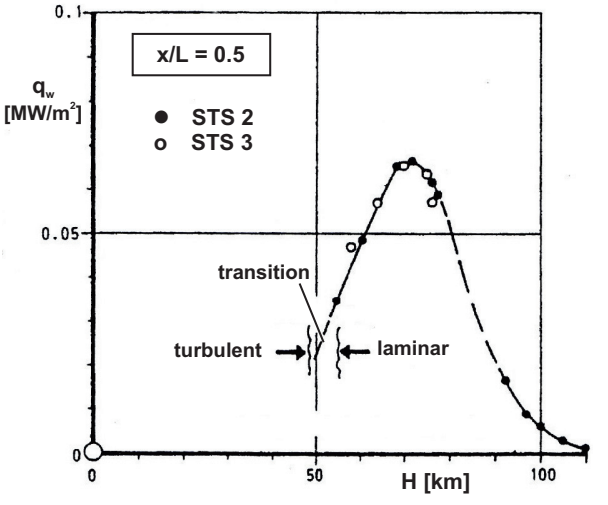

Fig. 2.6. Flight data of the heat flux in the gas at the wall, $q_w \equiv q_{gw}$, at $x/L = 0.5$ in the lower symmetry line of the Space Shuttle Orbiter [21]. Sources of data: 90 km $\lessapprox H \lessapprox$ 110 km: [22], 60 km $\lessapprox H \lessapprox$ 80 km: [23], laminar–turbulent transition domain: [24], $H \lessapprox$ 50 km: [25].

on a large part of the trajectory will fly at large angle of attack[19], Sub-Section 2.1.1. The heat flux depends also on some power of the wing loading W/A_{ref}. The larger the wing loading, the larger is q_{gw}.

– Eq. (2.27) can be used to guess the flight speed at which maximum heating occurs. Setting its differential with respect to the velocity ratio v_∞/v_c to zero:

$$\frac{dq_{gw}}{d(v_\infty/v_c)} = 0,$$

we obtain

$$\frac{v_\infty}{v_c}|_{q_{gw,max}} = \sqrt{\frac{m-2n}{m}}. \tag{2.28}$$

If we chose $n = 0.5$ and $m = 3$, the resulting velocity is with eq. (2.21) $v_\infty = 0.816\, v_c = 6{,}451.55$ m/s. This amounts, Fig. 2.2, to a flight altitude (STS-2) of approximately 70 km. Comparing this with flight data of the Space Shuttle Orbiter, Fig. 2.6, we find quite a good agreement.

This result must not be generalized. It holds for the lower side of the vehicle including the nose region at the trajectory part above 40–60 km altitude, where the attached viscous flow is laminar. Below that altitude

[19] We remember that also with a finite bank angle $\mu_a \neq 0$, the angle of attack α is kept, because the roll motion is made around the air-path or velocity vector.

range the viscous flow becomes turbulent[20] which leads to a strong increase of thermal loads. Depending on the considered trajectory, these can be equal or larger than those at approximately 70 km altitude with laminar flow. Data are available in this regard for the Space Shuttle Orbiter (see, e.g., [7]), where it is also shown that thermal loads (the heat flux in the gas q_{gw} at the wall) on the orbital maneuvering system (OMS) pod due to vortex interaction are largest for $\alpha \approx 20°$, which is an angle of attack typical for flight at an altitude of about 40–30 km.

– For the part of the trajectory with laminar flow, eq. (2.6) tells us directly, that flight at the same speed, but on a higher trajectory point ("lifting entry", Fig. 2.2), reduces the heating q_{gw} (and the dynamic pressure q_∞), because ρ_∞ decreases with increasing altitude. A lower trajectory point ("ballistic entry") at the same speed increases heating (and dynamic pressure).

Rearranging eq. (2.8) and assuming small γ and zero μ_a yields

$$v_\infty^2 = \frac{R_\infty}{m}(W - L). \tag{2.29}$$

If the aerodynamic lift L would be increased (visualize it with the help of Fig. 2.5), the flight altitude, here the radius of the flight path R_∞, must be increased, in order to keep v_∞ constant, and the vehicle flies at smaller density ρ_∞ and hence dynamic pressure q_∞ than before.

In general, increasing the lift, of course via $C_L(\alpha)$ and finally α, leads from a ballistic re-entry trajectory to a "higher" flight trajectory and hence can be used to reduce thermal loads on the flight vehicle[21], and to reduce the deceleration, via q_∞, which the vehicle undergoes during re-entry. It thus permits in addition larger down ranges and cross ranges.

– From eq. (2.26) a guess of the flight time can be made. Rearranging it yields:

$$t = -\frac{v_c}{2g_0}\frac{L}{D} ln\left(\frac{1 + v_\infty/v_c}{1 - v_\infty/v_c}\right). \tag{2.30}$$

Hence (with the time counted positive):

$$t \sim \frac{L}{D},$$

which indicates, that the larger L/D, the larger the flight time and, in addition, also the time-integrated heat flux $\overline{q}_{gw}$, eq. (2.2), if the effect is not compensated by fundamental trajectory changes.

[20] The accurate and reliable prediction of laminar–turbulent transition is still one of the large unsolved problems of fluid mechanics [5].

[21] This holds in any case for the nose region, but this effect can be configuration-dependent. Even higher thermal loads than at the nose can be present at other parts of a configuration, due to, for instance, thin boundary layers in strong expansion regions such as edges and shoulders. Hence a careful analysis is necessary in each case.

Reducing the flight time, and hence the time-integrated heat flux, can be achieved by reducing L/D. As we have seen above, this is not made via the angle of attack, but via the bank angle of the flight vehicle. Then the effective lift, eq. (2.12), is $L_{eff} = \cos\mu_a\, L < L$, and hence $L_{eff}/D < L/D$.

– Not only the flight time is proportional to the effective lift-to-drag ratio, but also the down range modulation capability:

$$\triangle x \sim \frac{L}{D}\cos\mu_a, \tag{2.31}$$

and the cross range:

$$\triangle y \sim \frac{L}{D}\sin\mu_a. \tag{2.32}$$

We see from these relations, that at given lift and drag the bank angle $\mu_a = 0$ gives the largest down range. To get a cross range modulation, a bank angle $\mu_a \neq 0$ is necessary. From eq. (2.32) $\mu_a = 90°$ appears to yield the largest cross range. However, actually that is achieved at $|\mu_a| = 45°$. We don't derive the exact relations, but refer the reader to, e.g., [18].

– The larger the drag D, the larger is the drag acceleration, eq. (2.20). The drag, like the lift, increases with increasing angle of attack α (rise of the effective bluntness), but stronger. This is the reason, why, at the large angles of attack flown during re-entry, L/D decreases with increasing α, Fig. 2.3.

– From eq. (2.8), also Fig. 2.5, we see that, due to the high speed of the vehicle and the curved flight path, on the initial trajectory—where γ is small—the aerodynamic lift L is small compared to the centrifugal force F_{centr}. The deceleration, eq. (2.20), see also eq. (2.7), however, is almost exclusively governed by the aerodynamic drag D.

Hence, if density uncertainties exist on a part of the trajectory, and $W\sin\gamma \ll D$, eq. (2.7), they will affect first of all the deceleration force, drag D, and hence dv_∞/dt. If the density on a larger part of the trajectory is smaller than assumed, this would lead, without corrective measures, to an increase of the down range.

The effect in general is large for RV-W's, which fly for a rather long time at small flight path γ (see, e.g., Fig. 2.10). In [26] it is indicated that in such a situation a density, which is 25 per cent smaller than initially assumed, would lead to an increase of the down range of approximately 100 km.

For RV-NW's, density uncertainties in general have smaller impact, because the flight interval with small γ is not so large (see, e.g., Fig. 2.9). However, even here we get for a 25 per cent uncertainty in ρ_∞ a down range change of about 50 km. This is large for a capsule, which has a small L/D and hence a restricted trajectory correction potential.

We have seen so far, that the basic aerodynamic lift-to-drag ratio L/D is mostly the important parameter. An increase of L/D in general can be desirable, for instance for arbitrary recall from orbit (requirement of flexible

down range) or large cross range demand, [9], even if constraints considerations (flight time, time-integrated heat flux) ask for a reduction of L to $L_{eff} < L$. However, in view of the small design experience base available, being in principle only that of the Space Shuttle Orbiter, one should be aware of the consequences of an increase of L/D regarding the choice and use of aerothermodynamic simulation means. This holds despite of the advances of the discrete numerical methods of aerothermodynamics which now seemingly allow to quantify more and more the aerothermodynamic properties of flight vehicles. The point is that ground-facility simulation remains for quite some time to come the major tool for data set generation, Sub-Section 1.2.2. This makes some further considerations necessary.

In the high angle of attack domain of re-entry flight, L/D can be increased by reducing α. If with the application of an advanced material, respectively thermal protection system, the nose radius R_N of a given RV-W-type flight vehicle could be reduced too, a further improvement of L/D would be possible, because this also reduces the wave drag. If pure surface radiation cooling of the nose region is demanded, of course, a trade-off becomes necessary between wave drag reduction and cooling effectiveness. Both wave drag and radiation cooling are reduced if the nose radius R_N is reduced [5].

Decreasing α and R_N thus can be used to optimize the aerodynamic performance of a re-entry vehicle within the limits of its structure and materials concept. It also can be used to reduce the thermal loads on the airframe via trajectory shaping [9]. However, if we reduce α on the high Mach number part of the trajectory, we move away from the benign wall (boundary-layer edge) Mach number interval, Sub-Section 3.6.4, on the windward side of the flight vehicle, and towards a Mach number and especially high temperature real gas sensitivity of aerodynamic coefficients, which is important in view of ground-facility simulation, Sub-Section 3.6.4.

We are also moving from the compressibility or pressure effects dominated RV-W in direction of the viscosity-effects dominated CAV. The more this happens, the more the proper simulation of viscous effects, including hypersonic viscous interaction phenomena, becomes important during the vehicle's definition and development process. Also thermo-chemical effects including finite-rate effects change their character. While thermo-chemical freezing phenomena in high-enthalpy ground-simulation facilities are in general not a major problem for a RV-W shape, like that of the Space Shuttle Orbiter, [5], this may change gradually for RV-W's with reduced α and R_N compared to that of the Space Shuttle Orbiter.

Increasing the aerodynamic performance L/D of a RV-W thus increases down range and cross range capabilities and in addition, via a large L, can decrease thermal loads, though not necessarily the time-integrated ones. However, the L/D increase changes the demands on the aerothermodynamic design with a kind of snow-ball effect which can be vicious.

Table 2.2. Characteristic quantities of APOLLO and SOYUZ capsules for the calculation of the trajectory in the planar limit.

Symbol	Quantity	APOLLO	SOYUZ
A_{ref}	reference area [m^2]	12.02	3.80
L/D	aerodynamic performance	0.30	0.26
C_L	lift coefficient	0.374	0.349
C_D	drag coefficient	1.247	1.341
m	total vehicle mass [kg]	5,470.0	2,400.0
V_e	flight velocity at entry [m/s]	7,670.0	7,900.0
γ_e	flight path angle at entry [°]	-0.75, -1.50, -3.50	-1.50
R_N	radius at stagnation point [m]	4.694	2.235

2.1.6 Case Study 1: Trajectories of RV-NW's

So far we have considered qualitative results derived from the relations for the equilibrium glide trajectory. We present now quantitative results for two RV-NW's. They are found from the numerical integration of the dynamic eqs. (2.7) and (2.8) together with the kinematic relations eqs. (2.9) and (2.10) corresponding to planar flight. We use simple relations for the gravitational acceleration $g(H)$, Appendix C,

$$g(H) = g_0 \left(\frac{R_E}{R_E + H} \right)^2, \tag{2.33}$$

and for the atmospheric density $\rho(H)$, Appendix B,

$$\rho(H) = \rho_0 e^{-\beta H}, \tag{2.34}$$

with $\beta = 1.40845 \cdot 10^{-4}$ m^{-1}.

Further we assume that the lift and the drag coefficient are constant along the whole trajectory. The stagnation point heat flux is calculated with eq. (10.76).

Investigated is the entry flight behavior of the APOLLO and the SOYUZ capsule. In Table 2.2 the characteristic quantities of both capsules, necessary for the computation of the trajectories, are listed. They are taken from Tables 5.1, 5.3, 5.4 and Figs. 5.11, 5.12.

In the first example the APOLLO trajectory for three values of the flight path angle at entry ($\gamma_e = -0.75°, -1.5°, -3.5°$) is considered. In Fig. 2.7 are plotted the altitude as function of the inertial velocity, a), and the inertial

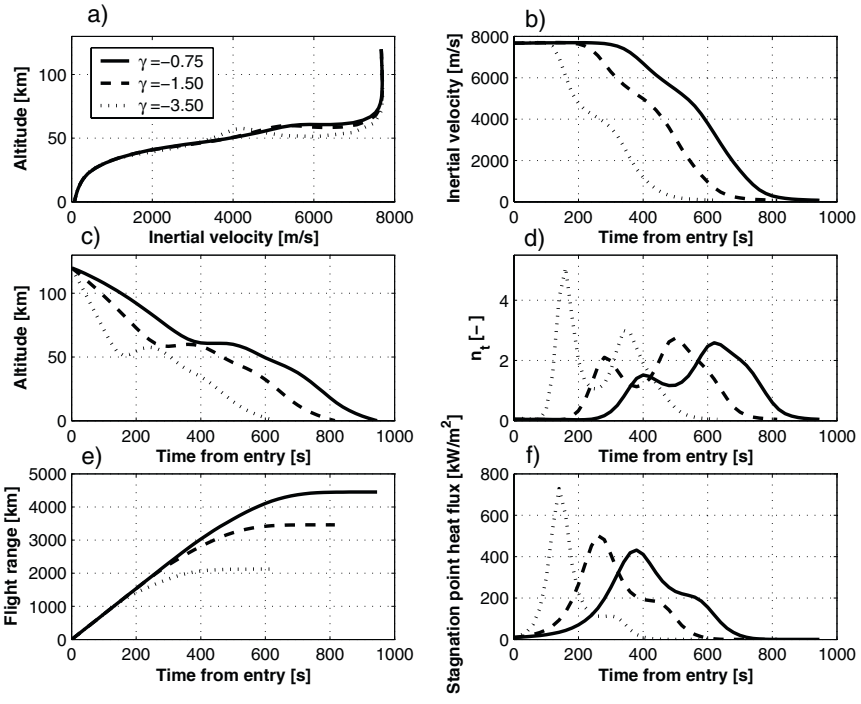

Fig. 2.7. APOLLO capsule: entry trajectory as function of the initial flight path angle γ_e based on planar equations.

velocity, the altitude, the normalized acceleration n_t, the flight range and the stagnation point heat flux as functions of time, b) to f).

The lowest entry flight path angle, $\gamma_e = -0.75°$, a value which is usually employed, leads to the smallest n_t and the smallest stagnation point heat flux, a), f), whereas the flight (down) range is largest, e). The largest angle, $\gamma_e = -3.5°$, produces a skip trajectory, which means that the flight path angle γ becomes positive over a certain distance with the consequence that the flight altitude grows, a), c). Further the g-loads and the stagnation point heat flux increase remarkable, d), f) while the flight range is lowest, e). Of course, the flight time is much smaller than for the lower γ_e values.

In the second example the trajectories of the APOLLO and the SOYUZ capsules are compared for the same flight path angle at entry ($\gamma_e = -1.5°$), Fig. 2.8. It seems that the tendency of SOYUZ for skipping is lower than for APOLLO, a). The maximum g-loads are reached at a later time, b), but the stagnation point heat flux is at the maximum higher and has a high value over a longer time interval leading to larger time-integrated thermal loads, d).

As mentioned in Appendix B, the density distribution in the atmosphere as function of the altitude is not constant but depends on the local and global

weather conditions. Therefore the question arises how density uncertainties on a part of the trajectory will affect the trajectory, see also Sub-Section 2.1.5. We test this with the APOLLO trajectory, Fig. 2.7, by multiplying the density function, eq. (2.33), once with 0.75 and then with 1.25.

Fig. 2.9 shows the result in terms of the flight path angle and the vehicle's deceleration. We can perceive that the density influence on the trajectory of a lifting capsule appears to be low, since the flight path angle anyway becomes soon large. The flight range for both the smaller and the larger value of the density function is only changed by approximately 1.2 per cent which, however, is large for a capsule.

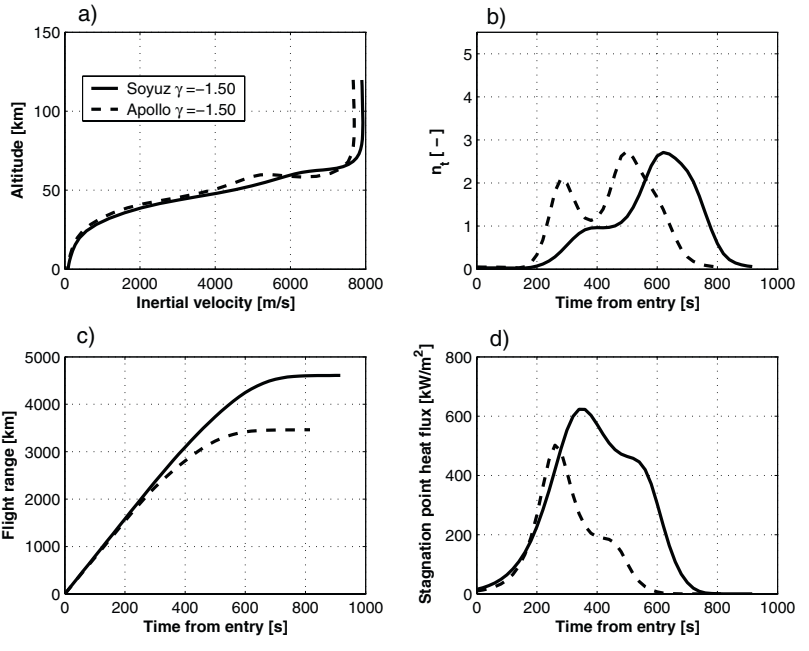

Fig. 2.8. APOLLO and SOYUZ capsule: comparison of entry trajectories based on planar equations.

2.1.7 Case Study 2: Trajectory of a RV-W (X-38)

In this case study we discuss the optimized trajectory of a RV-W, the X-38 [2]. The vehicle is to fly from an entry altitude of $H = 121.9$ km to the terminal area (TA) in the southwest of France, Fig. 2.10, upper right, arriving there at 24.1 km $\leqq H_{TA} \leqq$ 25.1 km with 645 m/s $\leqq v_{TA} \leqq$ 845 m/s. The guidance objective is the minimization of the time-integrated heat flux $\overline{q}_{gw}$.

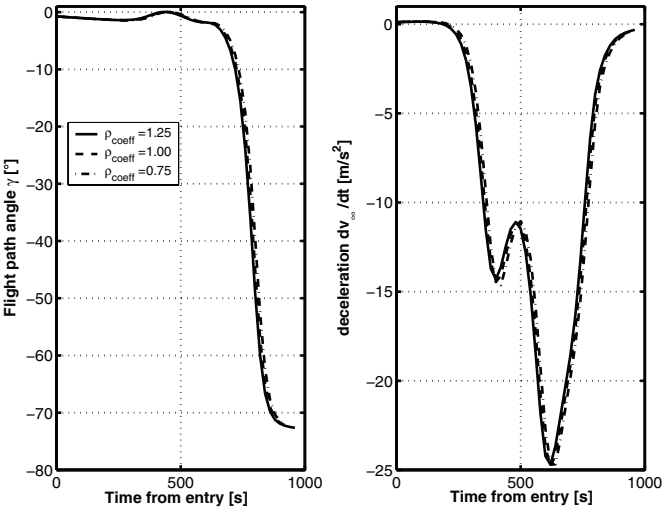

Fig. 2.9. APOLLO capsule: influence of atmospheric density variations on the flight trajectory. Flight path angle γ (left), vehicle deceleration dv_∞/dt (right).

Table 2.3. Systems and operational constraints of the X-38 flight [2].

q_∞	q_{gw}	n_z	γ	α
$\leqq$ 14.346 kPa	$\leqq$ 1,175 kW/m^2	$\leqq 2$	$\leqq 0°$	$35° \leqq \alpha \leqq 45°$

The determination of q_{gw} was made with eq. (10.76) in Section 10.3 for a nose radius $R_N = 0.3048$ m (= 1 ft). The control variables are the angle of attack α and the bank angle μ_a. The systems and operational constraints are given in Table 2.3.

We discuss summarily only some of the results. For the whole picture, including the definition of the guidance law, the reader is referred to [2].

The de-orbit maneuver generates an initial flight path angle of $\gamma \approx -1.6°$, Fig. 2.10, lower right. With a pull-up maneuver this angle is almost zeroed out[22] at the flight time $t = 322$ s. Then it drops to again $\gamma \approx -1.6°$ at $t \approx 880$ s. In this time interval the trajectory follows the $q_{gw} = q_{gw,max} = 1{,}750$ kW/m^2 constraint, Fig. 2.11. After a short rise the flight path angle drops to values around $\gamma \approx -10°$, and the trajectory follows the $n_z = n_{z,max} = 2$ constraint.

[22] An initial flight path angle of that magnitude would result in a trajectory initially too steep, with too large thermal loads and a large drag acceleration.

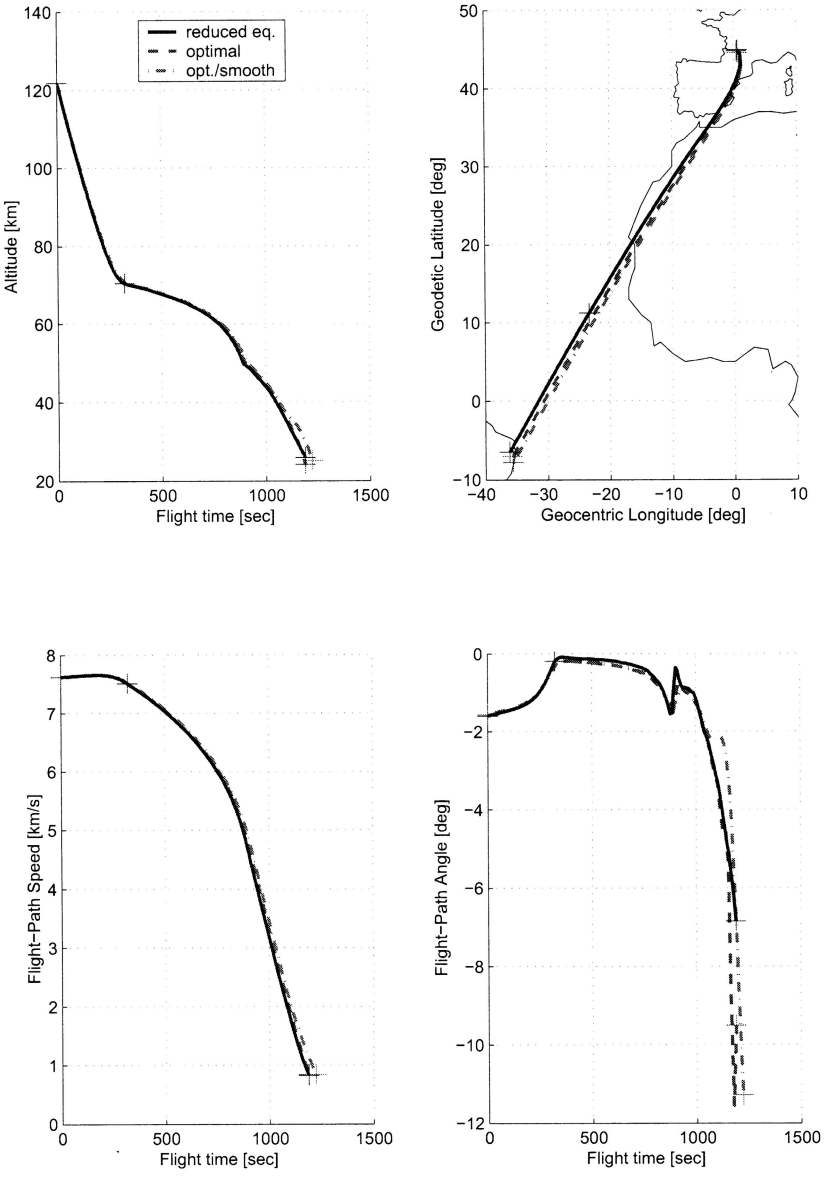

Fig. 2.10. Elements of the re-entry trajectory of the X-38 [2]. Upper left: flight altitude (H) as function of flight time (t). Upper right: ground track (the trajectory begins in this figure at the lower left and ends at the upper right). Lower left: flight path speed (v_∞) as function of flight time (t). Lower right: flight path angle (γ) as function of flight time (t).

In Fig. 2.11, upper part, this is reflected in the velocity/drag-acceleration map.[23] The trajectory, after the initial pull-up maneuver, down to $v_\infty \approx 5$ km/s follows the thermal load constraint and then down to $v_\infty \approx 2$ km/s that of the normal load factor. The dynamic pressure constraint $q_\infty = q_{\infty,max} =$ 14.346 kPa is approximately followed only for $v_\infty \lessapprox 2$ km/s. The drag acceleration of the resulting trajectory lies clearly above that of the equilibrium glide trajectory, the latter being characterized also by a much smaller dynamic pressure, Fig. 2.11, lower part.

The angle of attack, Fig. 2.12 (upper left, also to be read from the right to the left) down to $M_\infty \approx 10$ ($v_\infty \approx 3$ km/s) is the maximum angle $\alpha = \alpha_{max}$ $= 45°$. This high angle permits the large deceleration at minimum thermal loads while meeting the cross range demand. The bank angle μ_a, Fig. 2.12 (upper right) up to $t = 322$ s is zero in order to provide the lift needed for the pull-up maneuver. After that the effective aerodynamic lift is reduced by a large bank angle down to $\mu_a \approx -80°$, although without bank reversal, in order to reduce the flight time and thus the time-integrated heat flux $\overline{q}_{gw}$.

2.2 Flight Trajectories of Cruise and Acceleration Vehicles

2.2.1 General Aspects

In contrast to RV-W's and RV-NW's, CAV's have scarcely been flown. They are in general hypothetical vehicles and negligible flight experience is available. Airbreathing CAV's are to fly like ordinary airplanes. They are drag sensitive in contrast to RV-W's and RV-NW's, which need to employ a large aerodynamic drag to achieve their mission. Cruise vehicles and acceleration vehicles have different missions, Chapter 4, and hence different trajectory demands. We concentrate here somewhat on cruise-type vehicles, because several concepts of this kind have been studied in the recent past, mainly TSTO space transportation systems.

A CAV, if being the lower stage of a TSTO space-transportation system, usually is thought to perform a return-to-base mission ($A \rightarrow A$ flight). Hypersonic transport aircraft, in a sense also SSTO (ARV-type) vehicles, perform $A \rightarrow B$ flights. CAV's typically first employ turbojet propulsion (up to M_∞ ≈ 4), then, depending on the maximum flight Mach number, ramjet propulsion (up to $M_\infty \approx 7$) or combined ramjet/scramjet propulsion up to $M_\infty \approx$ 12–14. SSTO vehicles finally employ rocket propulsion to reach orbit. These different propulsion modes are an important issue in trajectory design and optimization, since at least for ramjet and scramjet propulsion a strong coupling of the propulsion forces, Fig. 2.14, into the force and moment balance of the vehicle exists, Sub-Section 2.2.3.

[23] The re-entry trajectory is beginning at a flight path speed of approximately 7.6 km/s, hence the figure must be read from the right to the left.

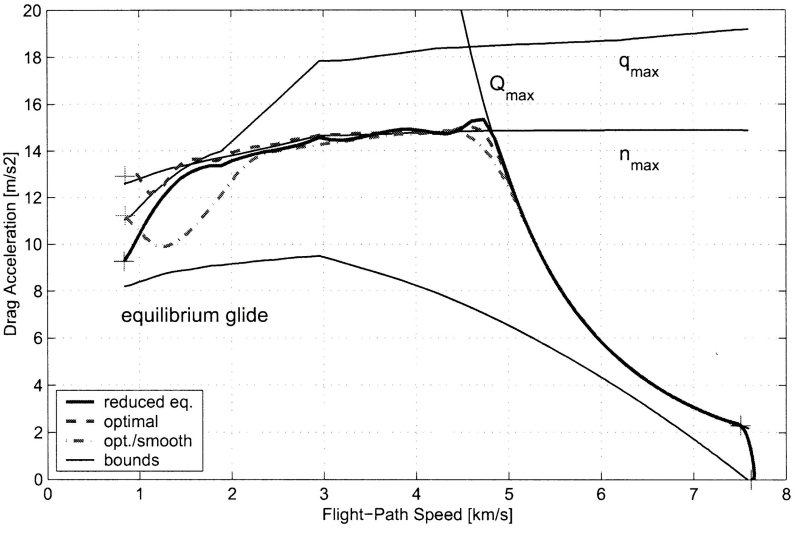

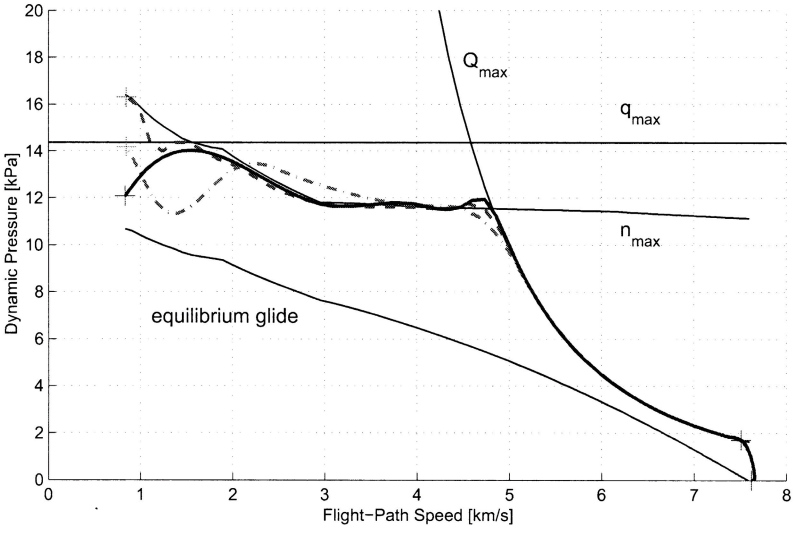

Fig. 2.11. Resulting trajectory representations [2]. Drag acceleration (D/m) as function of flight path speed (v_∞), and dynamic pressure (q_∞) as function of flight path speed (v_∞) (the trajectories begin at the lower right). The constraints are maximum values of dynamic pressure ($q_{max} \equiv q_{\infty,max}$), of heat flux in the gas at the wall ($Q_{max} \equiv q_{gw,max}$), and of the normal load factor ($n_{max} \equiv n_{z,max}$).

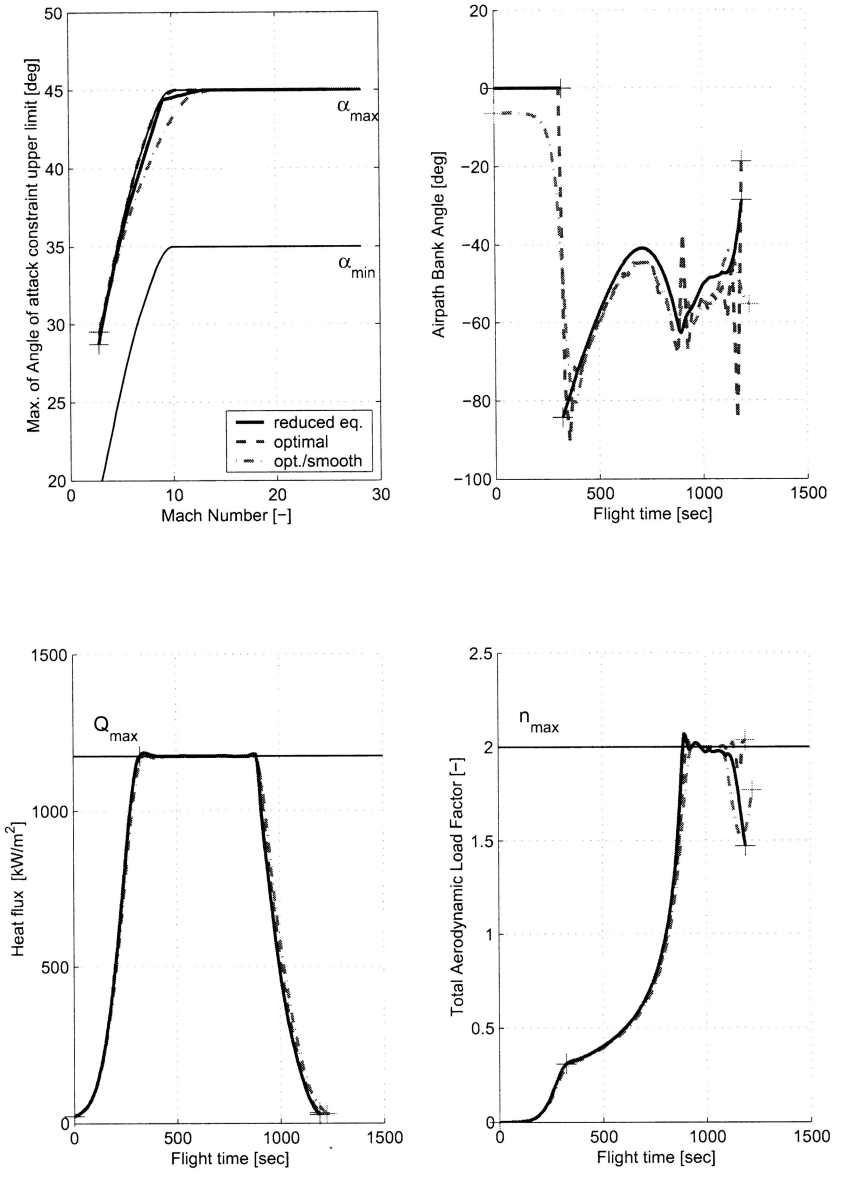

Fig. 2.12. Elements of the re-entry trajectory of the X-38 [2]. Upper left: maximum angle of attack (α_{max}) as function of flight Mach number (M_∞). Upper right: bank angle (μ_a) as function of flight time (t). Lower left: actual heat flux in the gas at the wall (q_{gw}) as function of flight time (t), $Q_{max} \equiv q_{gw,max}$. Lower right: actual normal load factor (n_z) as function of flight time (t), $n_{max} \equiv n_{z,max}$.

With TSTO or multistage systems another important issue is stage separation. It is characterized by the shedding of a large percentage of the system mass in a very short time interval, which leads to a large lift surplus of the carrier stage. This problem concerns flight dynamics, guidance and control and many other systems aspects.

A particular problem especially for large CAV's is the influence of aerothermoelasticity of the airframe and the aerodynamic control surfaces on the propulsion system performance, Sub-Section 4.5.4, and on the control properties of the flight vehicle. RV-W's (and RV-NW's) have rather stiff airframes, because of their cold primary (load-carrying) structures in combination with a TPS. This is not the case for large CAV's, where the airframe and the aerodynamic control surfaces may have, in addition to their large size, hot primary structures. The resulting additional couplings of aerodynamic, propulsion and control features will be highly dynamical and pose enormous design challenges (see, e.g., [27]), and also the present Sub-Section 4.5.4.

We restrict our discussion in the following sub-sections mostly to the issues of cruise-type vehicle trajectories in the turbojet/ramjet-propulsion domain without consideration of possible stage separation. We look at the guidance objectives, the trajectory control variables and the systems and operational constraints, extending the considerations of RV-W's and RV-NW's. The forces acting on a CAV are discussed, but, since no counterpart exists to the equilibrium glide of RV-W'sand RV-NW's, after that only a SÄNGER trajectory is considered as an example and some qualitative and quantitative results are presented.

2.2.2 Guidance Objectives, Trajectory Control Variables, and Systems and Operational Constraints

Guidance objectives. Guidance objectives are the optimization of vehicle performance, for instance:

- **Minimization of fuel consumption** for a given mission.
- **Maximization of total air-path energy** at upper stage separation of a TSTO space transportation system.
- **Maximization of pay load**, i. e., of the mass inserted into Earth orbit with a TSTO space transportation system.

Trajectory Control Variables. The number of trajectory control variables is, like that of RV-W's and RV-NW's, rather limited. The control variables are basically only:

- **Angle of attack** α, which governs aerodynamic lift L, drag D, and pitching moment M of the vehicle. It governs further, if forebody precompression is employed, Section 4.5, strongly the net thrust of the (air-breathing) propulsion system.

- **Power setting** of the propulsion system with its different engine modes.
- **Bank angle** μ_a of the vehicle (again, like for RV-W's, around the velocity vector $\mathbf{v}_\infty$). Banking is necessary for curved (in general $A \rightarrow A$) flight, and, in case of TSTO space transportation systems, to dump the surplus lift during stage separation.[24]

Systems and Operational Constraints. The basic systems and operational constraints are the same as, or similar to those of RV-W's and RV-NW's:

- The **dynamic pressure** q_∞ now is also a measure of the demands of the airbreathing propulsion system. The ascent trajectory of the SÄNGER TSTO system for instance was studied as a 50 kPa trajectory for both the turbojet and the ramjet mode [28]. If both the ramjet and the scramjet mode are to be employed, dynamic-pressure ranges of 25 kPa $\lessapprox q_\infty \lessapprox$ 95 kPa have been considered [27, 29].
- Flight of CAV-type vehicles below 40–60 km altitude means that the attached viscous flow predominantly is turbulent. The forward stagnation point however again is the primary reference location where **thermal loads** are constrained. In addition flat portions downstream of the nose region with turbulent flow may be chosen as reference locations.
- Besides the **normal load factor**, again with $n_{z,max} = 2$–2.5, the axial load factor with $n_{x,max} = q_\infty C_A A_{ref}/(m\,g) = 3$–$3.5$ is a constraint during the stage separation process of TSTO space transportation systems.
- Due to the influence of the thrust vector on the longitudinal forces and the pitching moment, Sub-Section 2.2.3, **trimmability**, and **stability and controllability** of the flight vehicle are critical operational constraints. If the thrust-force angle cannot be restricted or controlled mechanically, the only available degree of freedom to trim the vehicle is the symmetrical elevon deflection. If this angle is large, a substantial total drag D increase, due to the trim drag, will result. At the same time, depending on the overall forces and moment balance, a possible decrease of the lift L will happen, and an even stronger decrease of the lift-to-drag ratio L/D. Besides that the longitudinal stability characteristics of the vehicle will be influenced. Other issues in this regard are the resulting hinge moments (actuator performance) together with the mechanical and thermal loads on the elevons.

Besides these basic systems and operational constraints others may need to be prescribed, for instance regarding the airbreathing propulsion system.

[24] The mass of the upper stage of, for instance, the SÄNGER space transportation system, is at upper stage separation about one third of the total mass of the system. Hence when it leaves the lower stage, the latter has much too much lift, which immediately must be reduced in order to avoid collision with the upper stage, and to insure controllability of the flight vehicle.

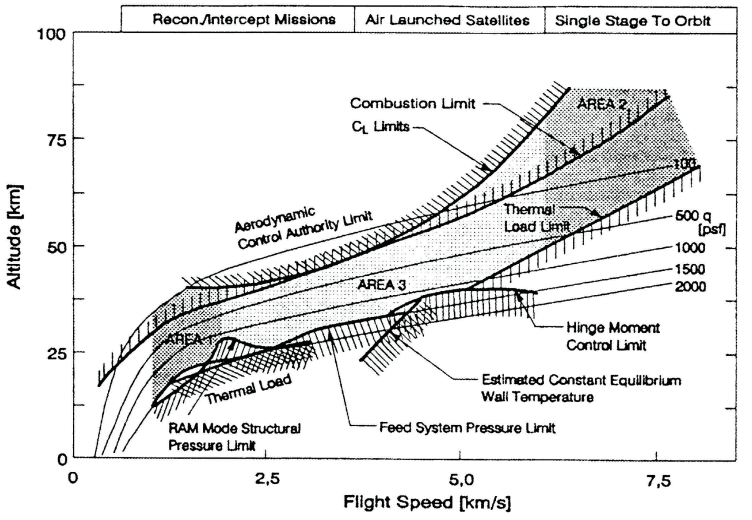

Fig. 2.13. Flight corridors and system and operational constraints of CAV-type flight vehicles in the altitude-velocity map [27].

A graphical presentation of the hypothetical flight corridor in the velocity-altitude map is given in Fig. 2.13, where Areas 1 and 3 concern for instance the lower stages of TSTO space transportation systems and hypersonic aircraft, whereas Area 2 concerns SSTO (ARV-type) systems.

The shaded flight corridor in Fig. 2.13 is bounded on the lower side by structural pressure limits and thermal loads of the airframe, the propulsion system and the control surfaces (hinge moment limit). On the upper side lift and combustion limits play a role and also the limit of the aerodynamic control authority. We have met the latter limit already with RV-W's. Control aspects possibly will make the flight corridor much narrower in reality, there might even be larger excluded regions due to propulsion issues [27].

In conclusion it can be stated that flight trajectory design and optimization for future large airbreathing CAV's poses extremely large challenges, much larger than those for RV-W's. Because Cayley's design paradigm, [30], see also the prologue to Chapter 8, is completely invalid for these vehicles, the highly non-linear aerodynamics/structure dynamics/propulsion/flight dynamics/flight control couplings make new vehicle design approaches necessary, but also new trajectory design and optimization approaches.

2.2.3 Forces Acting on a Cruise and Acceleration Vehicle

Again we approximate the flight vehicle as a point mass. A schematic point-mass force polygon of a propelled CAV is given in Fig. 2.14. Assumed is steady level flight, for non-steady flight the figure changes accordingly.

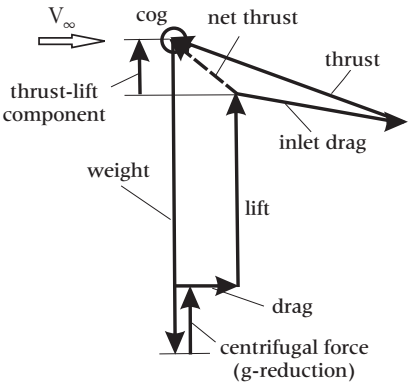

Fig. 2.14. Schematic point-mass force polygon at steady level flight of a propelled CAV [31].

The lower side of a CAV is a highly integrated lift and propulsion system [31]. Aerodynamic lift and propulsion provision are strongly coupled, Section 4.4. Depending on the thrust vector angle, a large net thrust lift component will exist. The net thrust is the—vectorial—difference between the inlet drag, i. e. the flow momentum entering the inlet of the propulsion system, and the thrust of the nozzle.

Since the nozzle is an asymmetric external nozzle[25], the thrust vector will change in magnitude and direction in a considerable range depending on flight speed, altitude, angle of attack and power setting of the propulsion system. The right-hand side figure of Fig. 2.15 is an example of the thrust vector angle as function of the flight Mach number. The jumps in the full lines in Fig. 2.15 of both the thrust coefficient and the thrust vector angle are due to the switch-over from the turbojet to the ramjet propulsion mode, which has not been smoothed out. The broken lines in Fig. 2.15 depict the data of the ejector nozzle. This nozzle dumps in the turbojet mode (up to $M_\infty = 3.5$) the forebody boundary layer material, which has been removed by the boundary layer diverter (see, e.g., [5]), into the main nozzle flow.[26]

On the left-hand side of Fig. 2.15 the axial thrust coefficient C_{FGX} is given. We see that around $M_\infty = 1$, in the transonic drag-rise domain, the C_{FGX} is smallest and the thrust vector angle $\triangle$ largest (negative). The latter leads (due to the need for trim) to a large elevon deflection[27] and hence to

[25] The classical bell nozzle of rocket propulsion cannot be integrated into the airframe of a CAV for thrust control (large flight Mach number span at not too large altitudes) and configurational reasons (see, e.g., [32]).

[26] It is not yet clear whether a boundary layer diverter is needed also in the ramjet and the scramjet propulsion mode.

[27] Whether a downward or an upward deflection is necessary depends on the actual location of the thrust vector acting line relative to the vehicle's center-of-gravity.

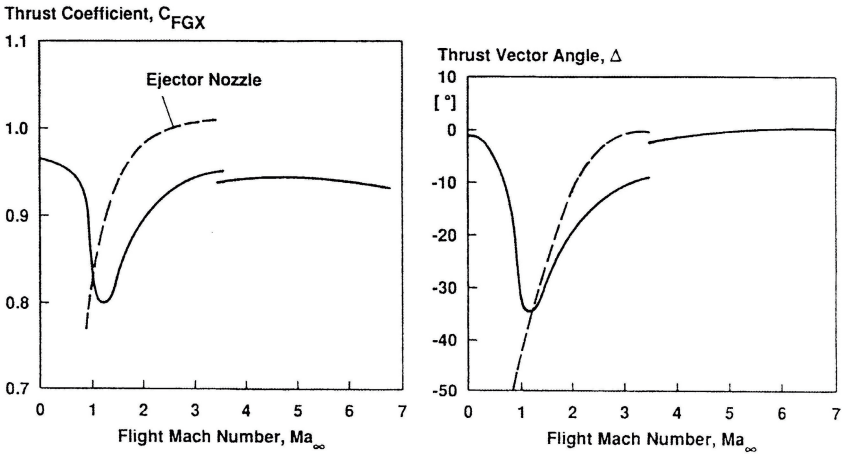

Fig. 2.15. Axial thrust coefficient C_{FGX} (left) and thrust vector angle $\triangle$ (right) as function of the flight Mach number Ma_∞ ($\equiv M_\infty$) of the SÄNGER lower stage [28] (nominal flight trajectory).

increased trim drag. To compensate in the transonic domain for both the decreased thrust (the thrust-lift component possibly is increased) and the increased drag, a transonic bunt maneuver[28] can be flown, where potential energy of the vehicle is exchanged for kinetic energy, Sub-Section 2.2.4.

Because usually forebody pre-compression is employed in order to reduce the inlet capture area, Section 4.5, a large dependence of the net thrust on the angle of attack is present. In reality this net thrust sensitivity will be enhanced by the forebody aerothermoelasticity (see, e.g., [33]), a problem, for which so far no solution has been found and which has not yet been accounted for in trajectory studies. The forebody pre-compression problem of a large CAV requires the quantification of the above mentioned highly non-linear aerodynamics/structure dynamics/propulsion/flight dynamics/flight control couplings of the vehicle.

2.2.4 Case Study 3: Trajectory of a CAV (SÄNGER)

We discuss now as example the optimized trajectory of the TSTO space transportation system SÄNGER [34]. The system is to fly from Southern Europe to the upper stage release at a northern latitude of 25° to 30° and back (return-to-base cruise). Again we look only at selected results.

The guidance objective is minimization of the fuel consumption for the whole mission, while the stage separation is to happen at $H = 33.35$ km altitude at $v_\infty = 2{,}085$ m/s with a flight path angle $\gamma = +8.5°$. The control variables are angle of attack α, the power (throttle) setting δ_T, and the

[28] The vehicle performs part of an inverted (or outside) loop.

bank angle μ_a. During the study the power setting δ_T for the ramjet mode ($M_\infty > 3.5$) was substituted by the fuel/air equivalence ratio[29] Φ_f, because overfueling (fuel-rich mixture) of ramjet combustion was found to have a favorable effect on the stage separation maneuver performance. The systems and operational constraints are given in Table 2.4. We note that also minimum constraints are prescribed, for instance for the dynamic pressure q_∞. This is necessary to assure minimum vehicle flyability and controllability and propulsion effectiveness.

Table 2.4. Systems and operational constraints of the SÄNGER flight [34].

	q_∞ $[kPa]$	α [°]	$\lvert\mu_a\rvert$ [°]	n_z	$\delta_{T,turbo}$	$\delta_{T,ram}$	$\Phi_{f,ram}$
Min:	10	-1.5	free	0	0	0	$\Phi_f(M_\infty, \delta_{T,min})$
Max:	50	20	prescribed	2	1	$\delta_T(M_\infty, \Phi_{f,max})$	3

A presentation of the resulting flight trajectory is given in Fig. 2.16. We observe some particularities of the trajectory [34]:

- The trajectory is a highly three-dimensional one with significant motion in longitudinal, vertical and lateral direction.
- The trajectory is throughout curved.
- In the transonic regime the drag increase, the large negative thrust vector angle $\triangle$, and the decrease of the axial thrust coefficient C_{FGX}, Sub-Section 2.2.3, make a bunt maneuver necessary (indicated at the far left of the ascent part of the trajectory, see also Fig. 2.17).
- The upper stage separation maneuver is characterized by a steep climb followed by a bunt, all reflected strongly in the control variables.

Fig. 2.17 shows that the flight up to the upper stage separation is an accelerated climb, and barely a cruise flight. The transonic bunt at $t \approx 200$ s is well discernible, similarly the stage separation maneuver at $t \gtrapprox 1{,}850$ s. The altitude oscillations in the trajectory parts before and after the stage separation are not due to numerical problems, but seem to be related to a phugoid-like motion [34].

The control variables are shown in Fig. 2.18. The angle of attack α does not change much before and after stage separation. The transonic bunt is

[29] The fuel/air equivalence ratio, usually called only equivalence ratio, is the ratio of the actual fuel/air ratio to the stoichiometric fuel/air ratio (see, e.g., [35]). The stoichiometric mixture hence has the equivalence ratio $\Phi_f = 1$. For hydrogen-fueled ramjets (and scramjets) a fuel-rich mixture ($\Phi_f > 1$) can be used to increase the thrust, which, of course, leads to an increase of the fuel consumption. A fuel-lean mixture ($\Phi_f < 1$) results in a decrease of fuel consumption.

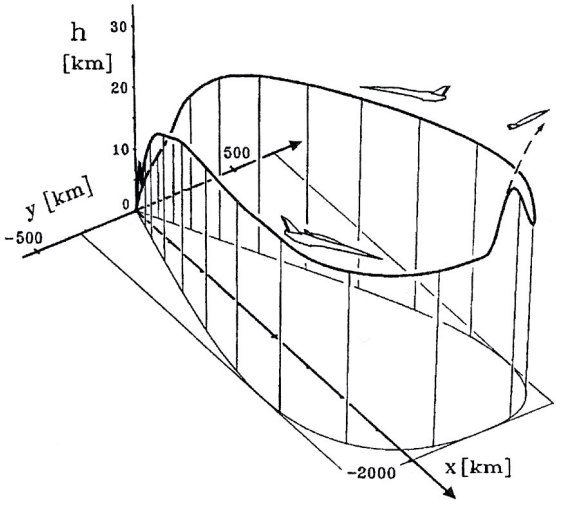

Fig. 2.16. The resulting return-to-base trajectory of the SÄNGER space transportation system in three-dimensions including upper stage separation [34].

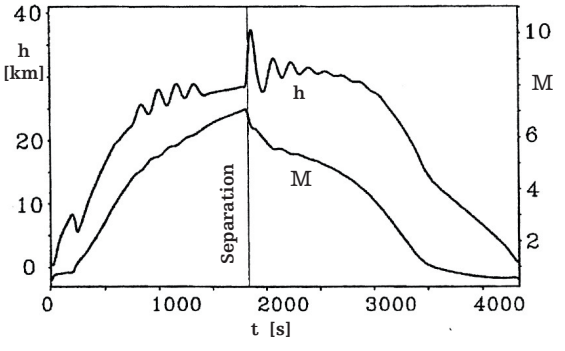

Fig. 2.17. Flight altitude h ($\equiv H$) and flight Mach number M ($\equiv M_\infty$) as function of flight time [34]. The separation of the upper stage is initiated at $t \approx 1{,}850.0$ s.

reflected, the pull-up for the stage separation maneuver demands a strong increase of α.

The power setting, respectively the equivalence ratio, is $\Phi_f \approx 1$ before stage separation. Transition from turbojet to ramjet propulsion—hardly observed in Fig. 2.18—is made between $M_\infty = 3$ to 3.5 ($t \approx 540$–600 s). A strong overfueling occurs prior to stage separation. On the return part of the trajectory Φ_f is much reduced, eventually to approximately zero, which amounts to a glide flight to base.

The bank angle μ_a (defined as negative to the left) increases steadily up to $-45°$, is zero during stage separation (wings level condition), and then drops to $\mu_a \approx -115°$. This happens in order to dump the excess lift after

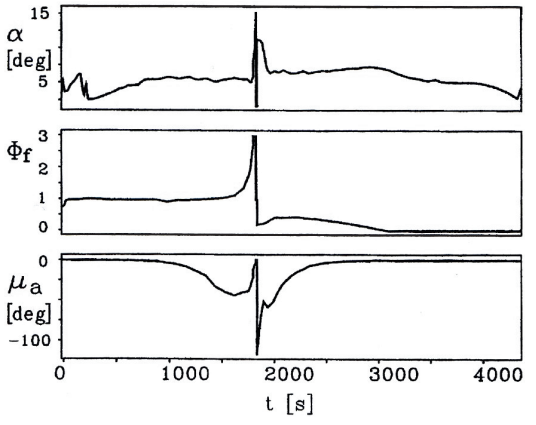

Fig. 2.18. The resulting trajectory control variables (from above): angle of attack α, equivalence ratio (power setting) Φ_f, bank angle μ_a as function of the flight time t [34].

upper stage release. Despite this the normal load factor (n_z) constraint is never violated.

Because the resulting large bank angle might not be acceptable for a large TSTO system, trajectories with bank angle limitation were also studied in [34]. The smaller the maximum permitted bank angle, the larger becomes the ground track of the trajectory, Fig. 2.19. Accordingly rises the fuel consumption, while on the return part of the trajectory the minimum dynamic-pressure constraint becomes active.

2.3 General Equations for Planetary Flight

Newton's second law is the basic equation valid for an inertial system, for example $\mathbf{O}, x_0, y_0, z_0$, Fig. 2.20, and reads:

$$m \left.\frac{d\underline{V}}{dt}\right|_0 = \underline{F}_{|0} = \underline{F}_{A\,|0} + m\underline{G}_{|0}, \tag{2.35}$$

where $\underline{F}_A$ contains the aerodynamic forces and $\underline{G}$ represents the gravity.[30] The planeto-centric coordinate system $\mathbf{p}$ rotates with the angular velocity $\underline{\bar{\Omega}}_{|p}$ around the origin $\mathbf{O}$ of the inertial system, Fig. 2.20. Therefore, applying the general rule for time derivatives of vectors in rotating systems, we find [16, 19]:

$$\left.\frac{d\underline{r}}{dt}\right|_0 = \left.\frac{d\underline{r}}{dt}\right|_p + \underline{\bar{\Omega}}_{|p} \times \underline{r}_{|p}, \quad \underline{\bar{\Omega}}_{|p} = \omega \begin{pmatrix} 0 \\ 0 \\ 1 \end{pmatrix}, \tag{2.36}$$

[30] Only unpowered flight is considered.

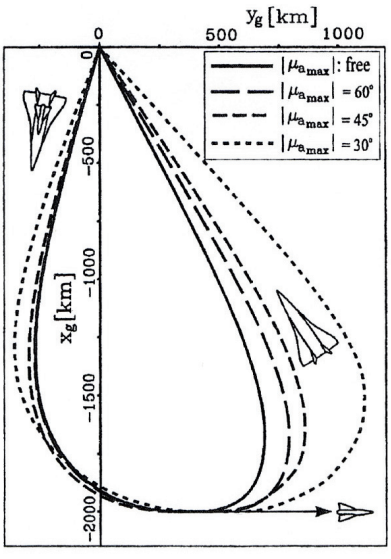

Fig. 2.19. The influence of the bank angle μ_a constraint on the resulting optimal cruise ground track [34].

and

$$\left.\frac{d\underline{V}}{dt}\right|_0 = \frac{d}{dt}(\underline{V}_{|p} + \underline{\bar{\Omega}}_{|p} \times \underline{r}_{|p}) + \underline{\bar{\Omega}}_{|p} \times (\underline{V}_{|p} + \underline{\bar{\Omega}}_{|p} \times \underline{r}_{|p}). \tag{2.37}$$

Since the angular velocity of the planet, $\underline{\bar{\Omega}}_{|p}$, is nearly a constant, we get with $d\underline{\bar{\Omega}}_{|p}/dt = 0$:

$$\left.\frac{d\underline{V}}{dt}\right|_0 = \left.\frac{d\underline{V}}{dt}\right|_p + 2\underline{\bar{\Omega}}_{|p} \times \underline{V}_{|p} + \underline{\bar{\Omega}}_{|p} \times (\underline{\bar{\Omega}}_{|p} \times \underline{r}_{|p}). \tag{2.38}$$

Combining eqs. (2.35) and (2.38) we obtain:

$$m\left.\frac{d\underline{V}}{dt}\right|_p = \underline{F}_{A\,|0} + m\underline{G}_{|0} - 2m\underline{\bar{\Omega}}_{|p} \times \underline{V}_{|p} - m\underline{\bar{\Omega}}_{|p} \times (\underline{\bar{\Omega}}_{|p} \times \underline{r}_{|p}). \tag{2.39}$$

We define the coordinate system **r**, which results from a rotation of the **p** coordinate system around the z_p axis, by θ and around the negative y_p axis by ϕ[31] such that x_r coincides with the position vector $\underline{r}$, Fig. 2.20. Further we need the coordinate system **g**, which is parallel to the **r** system, but with the origin **O'**, Fig. 2.21.

It is now our intention to formulate all the vectors used in the **g** coordinate system. The position vector $\underline{r}$ reads in the **p** coordinate system:

[31] The rotation around the negative y_p axis is identical with a rotation with $-\phi$.

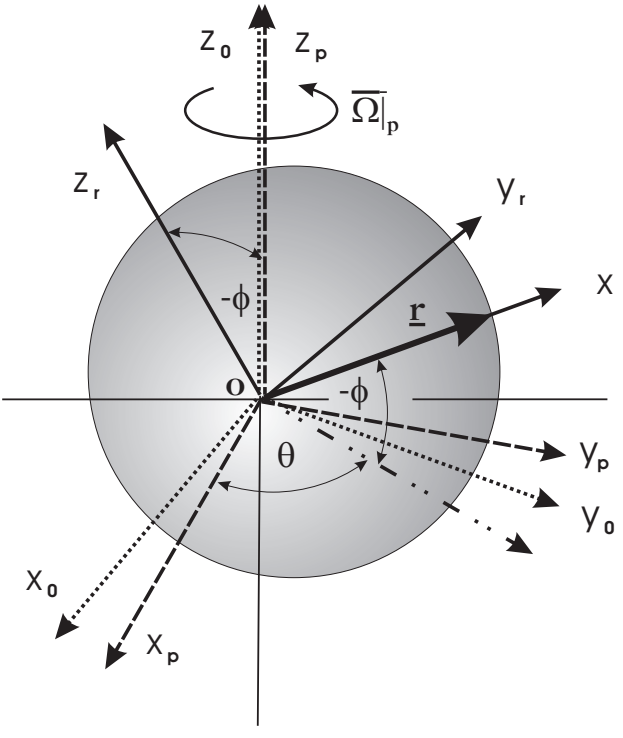

Fig. 2.20. Inertial coordinate system $\mathbf{O}, x_0, y_0, z_0$, planet fixed coordinate system $\mathbf{O}, x_p, y_p, z_p$ and rotating coordinate system $\mathbf{O}, x_r, y_r, z_r$.

$$\underline{r}\,|_p = r \begin{pmatrix} \cos\phi\cos\theta \\ \cos\phi\sin\theta \\ \sin\phi \end{pmatrix}. \tag{2.40}$$

With the matrices

$$M_{pg}^{-\phi} = \begin{pmatrix} \cos\phi & 0 & \sin\phi \\ 0 & 1 & 0 \\ -\sin\phi & 0 & \cos\phi \end{pmatrix}, \quad M_{pg}^{\theta} = \begin{pmatrix} \cos\theta & \sin\theta & 0 \\ -\sin\theta & \cos\theta & 0 \\ 0 & 0 & 1 \end{pmatrix}, \tag{2.41}$$

we transform $\underline{r}\,|_p$ and $\underline{\bar{\Omega}}\,|_p$ into the $\mathbf{g}$ coordinate system:

$$\underline{r}\,|_g = M_{pg}^{-\phi} M_{pg}^{\theta}\, \underline{r}\,|_p = r \begin{pmatrix} 1 \\ 0 \\ 0 \end{pmatrix}, \quad \underline{\bar{\Omega}}\,|_g = M_{pg}^{-\phi} M_{pg}^{\theta}\, \underline{\bar{\Omega}}\,|_p = \omega \begin{pmatrix} \sin\phi \\ 0 \\ \cos\phi \end{pmatrix}. \tag{2.42}$$

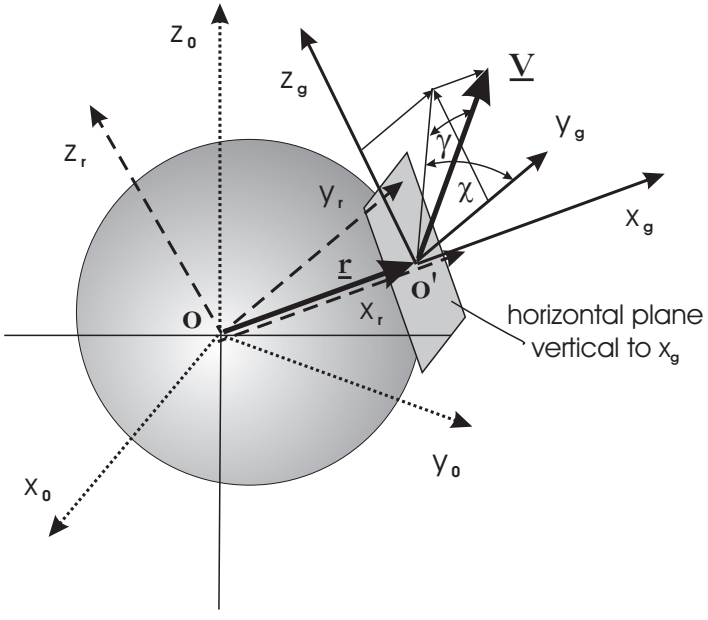

Fig. 2.21. Coordinate system **O'**, x_g, y_g, z_g parallel to coordinate system **O**, x_r, y_r, z_r.

The gravitational force in the **g** coordinate system is given by:

$$m\,\underline{G}_{|g} = mg \begin{pmatrix} -1 \\ 0 \\ 0 \end{pmatrix}. \tag{2.43}$$

The aerodynamic force $\underline{F}_A$ is composed of the drag $\underline{D}$, which is in opposite direction to the flight velocity $\underline{V}$, and the lift $\underline{L}$ which is perpendicular to this direction.

The velocity and the drag in the **g** coordinate system follow directly from Fig. 2.21, namely:

$$\underline{V}_{|g} = V \begin{pmatrix} \sin\gamma \\ \cos\gamma\cos\chi \\ \cos\gamma\sin\chi \end{pmatrix}, \quad \underline{D}_{|g} = -D \begin{pmatrix} \sin\gamma \\ \cos\gamma\cos\chi \\ \cos\gamma\sin\chi \end{pmatrix}. \tag{2.44}$$

We define now the coordinate system **k** (flight path system), where the velocity vector $\underline{V}_{|k}$ coincides with the y_k coordinate, Fig. 2.22.

Remark: The definitions of the coordinates x_g, y_g, z_g (**g**-frame) and x_k, y_k, z_k (**k**-frame), Figs. 2.21 and 2.22, are not in agreement with the tradition of notation associated with them. We apply this exception in order to make the

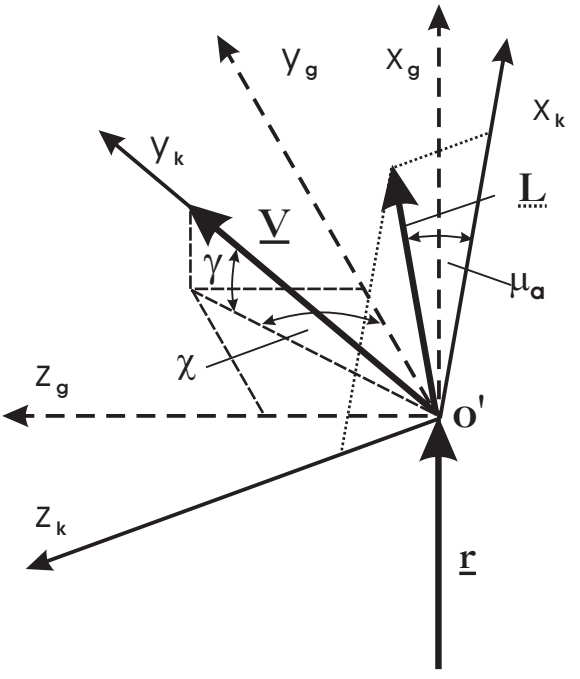

Fig. 2.22. Coordinate system **O'**, x_g, y_g, z_g and coordinate system **O'**, x_k, y_k, z_k (flight path) with the definition of bank angle μ_a and lift $\underline{L}$ outside the $\underline{r}, \underline{V}$ plane.

derivations and transformations easier to understand, having in mind that the scalar sets of eqs. (2.55) and (2.56) are independent of these definitions. Traditionally in the **g**-frame the coordinate z_g is directed vertically downwards, i.e. along the local g vector, and x_g and y_g are specified in any convenient way in the Earth horizontal plane. Further, in the **k**-frame the coordinate x_k is directed along the velocity vector $\underline{V}_{|k}$ and y_k lies in the Earth horizontal plane [16, 17].

With the matrices:

$$M_{gk}^{\gamma} = \begin{pmatrix} \cos\gamma & -\sin\gamma & 0 \\ \sin\gamma & \cos\gamma & 0 \\ 0 & 0 & 1 \end{pmatrix}, \quad M_{gk}^{\chi} = \begin{pmatrix} 1 & 0 & 0 \\ 0 & \cos\chi & \sin\chi \\ 0 & -\sin\chi & \cos\chi \end{pmatrix}, \tag{2.45}$$

we find

$$\underline{V}_{|k} = M_{gk}^{\gamma} M_{gk}^{\chi} \, \underline{V}_{|g} = V \begin{pmatrix} 0 \\ 1 \\ 0 \end{pmatrix}. \tag{2.46}$$

In planar flight the lift force $\underline{L}$ is in the $\underline{r}, \underline{V}$ plane, but for flight control and guidance purposes $\underline{L}$ is rotated out of this plane by an angle μ_a, Fig. 2.22. μ_a is the bank angle.

Therefore the directions of the coordinates of the **k** system coincide with $x_k \Rightarrow L \sin \mu_a$, $y_k \Rightarrow \underline{V}_{|k}$ and $z_k \Rightarrow L \cos \mu_a$, Fig. 2.22.

To transform the vector $\underline{L}_{|k}$ to the **g** coordinate system we have:

$$\underline{L}_{|g} = M_{kg}^{\chi} M_{kg}^{\gamma} \, \underline{L}_{|k}, \quad \underline{L}_{|k} = L \begin{pmatrix} \cos \mu_a \\ 0 \\ \sin \mu_a \end{pmatrix}, \tag{2.47}$$

where the matrix $M_{kg}^{\chi} M_{kg}^{\gamma}$ is the inverse of the matrix $M_{gk}^{\gamma} M_{gk}^{\chi}$ with

$$M_{kg}^{\gamma} = \begin{pmatrix} \cos\gamma & \sin\gamma & 0 \\ -\sin\gamma & \cos\gamma & 0 \\ 0 & 0 & 1 \end{pmatrix}, \quad M_{kg}^{\chi} = \begin{pmatrix} 1 & 0 & 0 \\ 0 & \cos\chi & -\sin\chi \\ 0 & \sin\chi & \cos\chi \end{pmatrix}. \tag{2.48}$$

In order to be able to formulate eq. (2.39) completely in the **g** coordinate system, we need finally for $d\underline{r}/dt_{|p}$ and $d\underline{V}/dt_{|p}$ the transformations from the **p** system to the **g** system, which have the forms:

$$\left.\frac{d\underline{r}}{dt}\right|_p = \left.\frac{d\underline{r}}{dt}\right|_g + \underline{\Omega}_{|g} \times \underline{r}_{|g}, \qquad \left.\frac{d\underline{V}}{dt}\right|_p = \left.\frac{d\underline{V}}{dt}\right|_g + \underline{\Omega}_{|g} \times \underline{V}_{|g}. \tag{2.49}$$

Here $\underline{\Omega}_{|g}$ denotes the vector of the rotation velocity of the **g** system relatively to the **p** system. Since the **g** coordinate system was obtained by rotations around the z_p and y_p axes with the Euler angles[32] θ and $-\phi$, Fig. 2.21, we find:

$$\underline{\Omega}_{|g} = M_{pg}^{-\phi} \begin{pmatrix} 0 \\ 0 \\ \dot{\theta} \end{pmatrix} + \begin{pmatrix} 0 \\ -\dot{\phi} \\ 0 \end{pmatrix} = \begin{pmatrix} \dot{\theta} \sin\phi \\ -\dot{\phi} \\ \dot{\theta} \cos\phi \end{pmatrix}, \tag{2.50}$$

$$\left.\frac{d\underline{r}}{dt}\right|_p = \frac{dr}{dt} \begin{pmatrix} 1 \\ 0 \\ 0 \end{pmatrix}_{|g} + \begin{pmatrix} 0 \\ \dot{\theta}\, r \cos\phi \\ \dot{\phi}\, r \end{pmatrix}_{|g} = \begin{pmatrix} \dot{r} \\ \dot{\theta}\, r \cos\phi \\ \dot{\phi}\, r \end{pmatrix}_{|g} = \underline{V}_{|g}. \tag{2.51}$$

Eqs. (2.44) and (2.51) represent the kinematic equations in the form (see also [19]):

$$\begin{aligned} \dot{r} &= V \sin\gamma, \\ \dot{\theta} &= \frac{V \cos\gamma \cos\chi}{r \cos\phi}, \\ \dot{\phi} &= \frac{V \cos\gamma \sin\chi}{r}. \end{aligned} \tag{2.52}$$

[32] For the definition of the Euler angles see [17] and Sub-Section 5.4.2.

All together we can write a compact form of the general flight mechanical equations for space applications in the **g** coordinate system:

$$m\left(\left.\frac{d\underline{V}}{dt}\right|_g + \underline{\Omega}_{|g} \times \underline{V}_{|g}\right) = \underline{D}_{|g} + M_{kg}^{\chi} M_{kg}^{\gamma} \underline{L}_{|k} + m\,\underline{G}_{|g} - \\ -2m\underline{\bar{\Omega}}_{|g} \times \underline{V}_{|g} - m\underline{\bar{\Omega}}_{|g} \times (\underline{\bar{\Omega}}_{|g} \times \underline{r}_{|g}). \quad (2.53)$$

By substitution of eqs. (2.42) to (2.44), (2.47), (2.50) into eq. (2.53) we obtain:

$$\frac{d}{dt} V \begin{pmatrix} \sin\gamma \\ \cos\gamma\cos\chi \\ \cos\gamma\sin\chi \end{pmatrix} + \begin{pmatrix} \dot{\theta}\sin\phi \\ -\dot{\phi} \\ \dot{\theta}\cos\phi \end{pmatrix} \times V \begin{pmatrix} \sin\gamma \\ \cos\gamma\cos\chi \\ \cos\gamma\sin\chi \end{pmatrix} = \\ -\frac{1}{m} D \begin{pmatrix} \sin\gamma \\ \cos\gamma\cos\chi \\ \cos\gamma\sin\chi \end{pmatrix} + \frac{1}{m} L \begin{pmatrix} \cos\gamma\cos\mu_a \\ -\sin\gamma\cos\chi\cos\mu_a - \sin\chi\sin\mu_a \\ -\sin\gamma\sin\chi\cos\mu_a + \cos\chi\sin\mu_a \end{pmatrix} + \\ + g \begin{pmatrix} -1 \\ 0 \\ 0 \end{pmatrix} - 2\omega \begin{pmatrix} \sin\phi \\ 0 \\ \cos\phi \end{pmatrix} \times V \begin{pmatrix} \sin\gamma \\ \cos\gamma\cos\chi \\ \cos\gamma\sin\chi \end{pmatrix} - \\ - \omega \begin{pmatrix} \sin\phi \\ 0 \\ \cos\phi \end{pmatrix} \times \left\{ \omega \begin{pmatrix} \sin\phi \\ 0 \\ \cos\phi \end{pmatrix} \times r \begin{pmatrix} 1 \\ 0 \\ 0 \end{pmatrix} \right\}. \quad (2.54)$$

Resolving eq. (2.54) for dV/dt, $Vd\gamma/dt$, $Vd\chi/dt$ by using the relations of eq. (2.52) leads to, (see also [19]):

$$\begin{aligned} \frac{dV}{dt} &= -\frac{1}{m} D - g\sin\gamma + \omega^2 r\cos^2\phi(\sin\gamma - \cos\gamma\tan\phi\sin\chi), \\ V\frac{d\gamma}{dt} &= \frac{1}{m} L\cos\mu_a - g\cos\gamma + \frac{V^2}{r}\cos\gamma + 2\omega V\cos\phi\cos\chi + \\ &\quad + \omega^2 r\cos^2\phi(\cos\gamma + \sin\gamma\tan\phi\sin\chi), \\ V\frac{d\chi}{dt} &= \frac{1}{m}\frac{L\sin\mu_a}{\cos\gamma} - \frac{V^2}{r}\cos\gamma\cos\chi\tan\phi + \\ &\quad + 2\omega V(\tan\gamma\cos\phi\sin\chi - \sin\phi) - \frac{\omega^2 r}{\cos\gamma}\sin\phi\cos\phi\cos\chi. \quad (2.55) \end{aligned}$$

These are the force equations which describe the unpowered motion of aerospace vehicles during space flight including ascent and descent. Since ω is a small value, generally the influence of the term $\omega^2 r$ is low. More important is the quantity $2\omega V$, which describes the influence of the Coriolis forces, which aerospace vehicles experience moving relative to a rotating system. The impact of this term diminishes for flights along descent trajectories with strong deceleration.

By considering the planet as non-rotating we have $\omega = 0$, and the **p** coordinate system takes over the role of the inertial system. Eq. (2.55) then reduces to:

$$\begin{aligned}
\frac{dV}{dt} &= -\frac{1}{m}D - g\sin\gamma, \\
V\frac{d\gamma}{dt} &= \frac{1}{m}L\cos\mu_a - g\cos\gamma + \frac{V^2}{r}\cos\gamma, \\
V\frac{d\chi}{dt} &= \frac{1}{m}\frac{L\sin\mu_a}{\cos\gamma} - \frac{V^2}{r}\cos\gamma\cos\chi\tan\phi.
\end{aligned} \tag{2.56}$$

For flight, where the flight path azimuth angle χ is not changed, the third of the scalar equations, eq. (2.56), vanishes and we have the relations given at the beginning of Sub-Section 2.1.4.

Remark: It should be noted that eqs. (2.55) with the $2\omega V$- and the $\omega^2 r$- terms are only valid in the inertial **O**-frame, while eqs. (2.56) are to be applied on the basis of the **p**-frame as inertial system. Actually the magnitude of V, describing the same planetary or orbital flight situation, is different in both frames and hence in both sets of equations.

For clarification we define an example. Let us assume that a space vehicle moves along an equatorially circular orbit around the Earth, which is determined—as is well known—by the balance of the gravitational and the centrifugal forces. The velocity of the space vehicle in the **p**-frame is then given by:

$$V_{circ} = \left[(R_E + H)g(H)\right]^{1/2}. \tag{2.57}$$

The velocity in a point on this circular orbit due to the Earth rotation is:

$$V_E = \omega(R_E + H). \tag{2.58}$$

This means that the determination of the velocity of a vehicle along this circular orbit, using eq. (2.56), has to be made with:

$$V^p_{|g} = V_{circ},$$

and, using eq. (2.55), with:

$$V^0_{|g} = V_{circ} - V_E,$$

see Problem 2.5.

2.4 Problems

Problem 2.1. Calculate flight velocity and Mach number of the Space Shuttle Orbiter in connection with the RCS employment during re-entry flight for a) $q_\infty = 0.48$ kPa at 81 km altitude and b) $q_\infty = 1.9$ kPa at 69 km altitude.

Problem 2.2. The maximum heat flux at the lower symmetry line at $x/L = 0.5$ of the Space Shuttle Orbiter given in Fig. 2.6 is $(q_w =)\, q_{gw} = 0.067\,\mathrm{MW/m^2}$. Assume zero heat flux into the wall and no other heat-flux contributions. How large is the radiation-adiabatic temperature belonging to that heat flux, if $\varepsilon = 0.85$?

Problem 2.3. How large is the heat flux in the gas at the wall, q_{gw}, at the vehicle nose for the flight conditions of Problem 2, assuming $H = 70$ km and $v_\infty = 6{,}450$ m/s? Assume an effective nose radius of $R_N = 1.3$ m. Use the simplest relation for q_{gw} given in Section 10.3. Is the heat flux within the usual constraints? How large is T_{ra}, if $\varepsilon = 0.85$? Is it acceptable from the material point-of-view?

Problem 2.4. Repeat Problem 2.3 for an effective nose radius $R_N = 0.25$ m. Are the heat flux and T_{ra} acceptable?

Problem 2.5. a) At what altitude H is an equatorially circular orbit synchronized with the Earth rotation, saying that the position of a space vehicle is fixed with respect to an observer on the Earth surface? b) How large is the velocity magnitude V, when the simulation of the flight of a vehicle in this orbit is made with eqs. (2.55) and alternatively with eqs. (2.56)?

Assume that the gravitational acceleration is given by $g = g_0[R_E/(R_E + H)]^2$.

References

1. Harpold, J.C., Graves Jr., C.A.: Shuttle Entry Guidance. In: Proc. 25th Anniversary Conference of the American Astronomical Society (AAS 78-147), pp. 99–132 (1978)
2. Markl, A.W.: An Initial Guess Generator for Launch and Reentry Vehicle Trajectory Optimization. Doctoral Thesis, Universität Stuttgart, Germany (2001)
3. Adams, J.C., Martindale, W.R., Mayne, A.W., Marchand, E.O.: Real Gas Scale Effects on Hypersonic Laminar Boundary-Layer Parameters Including Effects of Entropy-Layer Swallowing. AIAA-Paper 76-358 (1976)
4. Wüthrich, S., Sawley, M.L., Perruchoud, G.: The Coupled Euler/ Boundary-Layer Method as a Design Tool for Hypersonic Re-Entry Vehicles. Zeitschrift für Flugwissenschaften und Weltraumforschung (ZFW) 20(3), 137–144 (1996)
5. Hirschel, E.H.: Basics of Aerothermodynamics. Progress in Astronautics and Aeronautics, AIAA, Reston, Va, vol. 204. Springer, Heidelberg (2004)
6. Williams, S.D.: Columbia, the First Five Flights Entry Heating Data Series, an Overview, vol. 1. NASA CR-171 820 (1984)
7. Hoey, R.G.: AFFTC Overview of Orbiter-Reentry Flight-Test Results. In: Arrington, J.P., Jones, J.J. (eds.) Shuttle Performance: Lessons Learned. NASA CP-2283, Part 2, pp. 1303–1334 (1983)
8. Koelle, D.E., Kuczera, H.: SÄNGER – An Advanced Launcher System for Europe. IAF-Paper 88-207 (1988)
9. Neumann, R.D.: Defining the Aerothermodynamic Methodology. In: Bertin, J.J., Glowinski, R., Periaux, J. (eds.) Hypersonics. Defining the Hypersonic Environment, vol. 1, pp. 125–204. Birkhäuser, Boston (1989)
10. Haney, J.W.: Orbiter (Pre STS-1) Aeroheating Design Data Base Development Methodology: Comparison of Wind Tunnel and Flight Test Data. In: Throckmorton, D.A. (ed.) Orbiter Experiments (OEX) Aerothermodynamics Symposium. NASA CP-3248, Part 2, pp. 607–675 (1995)

11. American National Standards Institute. Recommended Practice for Atmosphere and Space Flight Vehicle Coordinate Systems. American National Standard ANSI/AIAA R-0004-1992 (1992)
12. Romere, P.O.: Orbiter (Pre STS-1) Aerodynamic Design Data Book Development and Methodology. In: Throckmorton, D.A. (ed.) Orbiter Experiments (OEX) Aerothermodynamics Symposium. NASA CP-3248, Part 1, pp. 249–280 (1995)
13. Iliff, K.W., Shafer, M.F.: Extraction of Stability and Control Derivatives from Orbiter Flight Data. In: Throckmorton, D.A. (ed.) Orbiter Experiments (OEX) Aerothermodynamics Symposium. NASA CP-3248, Part 1, pp. 299–344 (1995)
14. McCormick, B.W.: Aerodynamics, Aeronautics, and Flight Mechanics. John Wiley & Sons, New York (1979)
15. Schlichting, H., Truckenbrodt, E.: Aerodynamik des Flugzeuges. Teil I. Springer, Berlin (1967)
16. Etkin, B.: Dynamics of Atmospheric Flight. John Wiley & Sons, New York (1972)
17. Brockhaus, R.: Flugregelung. Springer, Heidelberg (2001)
18. Hankey, W.L.: Re-Entry Aerodynamics. AIAA Education Series, Washington, D.C (1988)
19. Vinh, N.X., Busemann, A., Culp, R.D.: Hypersonic and Planetary Entry Flight Mechanics. The University of Michigan Press, Ann Arbor (1980)
20. Regan, F.J.: Re-Entry Vehicle Dynamics. AIAA Education Series, Washington, D. C (1984)
21. Hirschel, E.H.: Aerodynamische Probleme bei Hyperschall-Fluggeräten. Jahrestagung der DGL (October 9 and 10, 1986) München, Germany, also MBB/S/PUB/270, MBB, München/Ottobrunn, Germany (1986)
22. Shinn, J.L., Simmonds, A.L.: Comparison of Viscous Shock-Layer Heating Analysis with Shuttle Flight Data in Slip Flow Regime. AIAA-Paper 84-0226 (1984)
23. Zoby, E.V., Gupta, R.N., Simmonds, A.L.: Temperature-Dependent Reaction-Rate Expression for Oxygen Recombination at Shuttle Entry Conditions. AIAA-Paper 84-0224 (1984)
24. Goodrich, W.D., Derry, S.M., Bertin, J.J.: Shuttle Orbiter Boundary-Layer Transition: A Comparison of Flight and Wind Tunnel Data. AIAA-Paper 83-0485 (1983)
25. Gupta, R.N., Moss, J.N., Simmonds, A.L., Shinn, J.L., Zoby, E.V.: Space Shuttle Heating Analysis with Variation in Angle of Attack and Surface Condition. AIAA-Paper 83-0486 (1983)
26. Kuczera, H.: Bemannte europäische Rückkehrsysteme – ein Überblick. Space Course, Vol. 1, Universität Stuttgart, Germany, pp. 161–172 (1995)
27. McRuer, D.: Design and Modelling Issues for Integrated Airframe/Propulsion Control of Hypersonic Flight Vehicles. In: Proc. American Control Conference, Boston, Mass., pp. 729–735 (1991)
28. Hauck, H.: Leitkonzept SÄNGER – Referenz-Daten-Buch. Issue 1, Revision 2, Dasa, München/Ottobrunn, Germany (1993)
29. Hunt, J.L.: Hypersonic Airbreathing Vehicle Design (Focus on Aero-Space Plane). In: Bertin, J.J., Glowinski, R., Periaux, J. (eds.) Hypersonics. Defining the Hypersonic Environment, vol. 1, pp. 205–262. Birkhäuser, Boston (1989)
30. Hirschel, E.H.: Towards the Virtual Product in Aircraft Design? In: Periaux, J., Champion, M., Gagnepain, J.-J., Pironneau, O., Stouflet, B., Thomas, P.

(eds.) Fluid Dynamics and Aeronautics New Challenges. CIMNE Handbooks on Theory and Engineering Applications of Computational Methods, Barcelona, Spain, pp. 453–464 (2003)
31. Hirschel, E.H.: Aerothermodynamic Phenomena and the Design of Atmospheric Hypersonic Airplanes. In: Bertin, J.J., Periaux, J., Ballmann, J. (eds.) Advances in Hypersonics. Defining the Hypersonic Environment, vol. 1, pp. 1–39. Birkhäuser, Boston (1992)
32. Edwards, C.L.W., Small, W.J., Weidner, J.P.: Studies of Scramjet/Airframe Integration Techniques for Hypersonic Aircraft. AIAA-Paper 75-58 (1975)
33. Hirschel, E.H.: The Technology Development and Verification Concept of the German Hypersonics Technology Programme. AGARD R-813, pp. 12-1–12-15 (1986)
34. Bayer, R., Sachs, G.: Optimal Return-to-Base Cruise of Hypersonic Carrier Vehicles. Zeitschrift für Flugwissenschaften und Weltraumforschung (ZFW) 19(1), 47–54 (1992)
35. Heiser, W.H., Pratt, D.T.: Hypersonic Airbreathing Propulsion. AIAA Education Series, Washington, D.C (1994)